







Strong laser fields and their power to generate controllable high-photon-number coherent-state superpositions

J. Rivera-Dean ¹, Th. Lamprou,^{2,3} E. Pisanty ^{1,4,5}, P. Stammer,^{1,4} A. F. Ordóñez,¹ A. S. Maxwell ^{1,6},
M. F. Ciappina ^{1,7,8}, M. Lewenstein ^{1,9,*} and P. Tzallas ^{2,10,†}

¹ICFO–Institut de Ciències Fotoniques, The Barcelona Institute of Science and Technology, 08860 Castelldefels (Barcelona), Spain

²Foundation for Research and Technology–Hellas, Institute of Electronic Structure & Laser, GR-70013 Heraklion (Crete), Greece

³Department of Physics, University of Crete, P.O. Box 2208, GR-71003 Heraklion (Crete), Greece

⁴Max Born Institute for Nonlinear Optics and Short Pulse Spectroscopy, Max Born Strasse 2a, D-12489 Berlin, Germany

⁵Department of Physics, King's College London, WC2R London, United Kingdom

⁶Department of Physics and Astronomy, Aarhus University, DK-8000 Aarhus C, Denmark

⁷Physics Program, Guangdong Technion–Israel Institute of Technology, 241 Daxue Road, Shantou, Guangdong 515063, China

⁸Technion–Israel Institute of Technology, Haifa 32000, Israel

⁹ICREA, Pg. Lluís Companys 23, 08010 Barcelona, Spain

¹⁰ELI–ALPS, ELI–Hu Non-Profit Ltd., Dugonics tér 13, H-6720 Szeged, Hungary



(Received 18 October 2021; revised 23 February 2022; accepted 25 February 2022; published 23 March 2022)

Recently, intensely driven laser-matter interactions have been used to connect the fields of strong laser field physics with quantum optics by generating nonclassical states of light. Here, we take a further key step and show the potential of strong laser fields for generating controllable high-photon-number coherent-state superpositions. This has been achieved by using two of the most prominent strong-laser induced processes: high-harmonic generation and above-threshold ionization. We show how the obtained coherent-state superpositions change from an optical Schrödinger “cat” state to a “kitten” state by changing the atomic density in the laser-atom interaction region, and we demonstrate the generation of a nine-photon shifted optical “cat” state, which, to our knowledge, is the highest photon number optical “cat” state experimentally reported. Our findings anticipate the development of new methods that naturally lead to the creation of high-photon-number controllable coherent-state superpositions, advancing investigations in quantum technology.

DOI: [10.1103/PhysRevA.105.033714](https://doi.org/10.1103/PhysRevA.105.033714)

I. INTRODUCTION

Strong laser field physics and quantum optics are two research directions founded on the classical and quantum description of the electromagnetic field, respectively. Quantum optics has proven to be a very important field in the development of quantum technologies [1–3], advancing studies ranging from fundamental tests of quantum theory to quantum information processing and quantum communication protocols. Central to these applications lies the concept of nonclassical light states, that is, states of light that can be described only in a quantum-mechanical frame [4–6]. Within the family of nonclassical light states, the superposition of two distinct coherent states, i.e., the so-called optical *Schrödinger cat states*, has proven to be a potentially useful candidate for the aforementioned applications [7–12]. However, despite the progress there has been so far towards their practical generation [13–18], the applicability of the existing optical cat states is partially restricted by their low photon number. Furthermore, the development of new schemes for the generation

of high-photon-number optical cat states with controllable quantum features is considered a challenging task.

On the other hand, strong laser field physics [19–25] is a widely active research direction that has opened the way for studies ranging from relativistic electron acceleration (see [19] and references therein) to ultrafast electronics (see [26–28] and references therein). Central to these investigations is the interaction of atoms with intense laser fields, which leads to the generation of coherent radiation in the extreme ultraviolet (XUV) [23,29–34] and the x-ray [35,36] regimes, and it has been substantially applied in attosecond science [23,27,37], nonlinear XUV optics [38–45], high-resolution spectroscopy [46,47], and tomography [48,49]. The majority of these studies are experimentally conducted using high-power femtosecond laser sources, and their interaction with matter is theoretically described by approaches in which the electromagnetic field is treated classically.

Despite the large amount of progress achieved in quantum optics and strong laser field physics, the direction of both research domains has remained uncoupled over the years. This is primarily due to the highly successful treatment of a classical electromagnetic field in strong laser physics and the assumption that the quantum aspects of the field were superfluous. Thus, the advantages emerging from the connection between quantum optics and strong laser field physics remain

*maciej.lewenstein@icfo.eu

†ptzallas@iesl.forth.gr

largely unexploited. However, very recently a link between both disciplines has been achieved theoretically and experimentally by showing that intense laser-matter interactions can lead to the generation of optical Schrödinger cat states [50].

Here, we take a key step forward and show the power of the strong laser fields for the generation of controllable high-photon-number coherent-state superpositions. This has been achieved using the processes of high-harmonic generation (HHG) and above-threshold ionization (ATI) induced in intense laser-atom interactions. Specifically, we study the back-action of these two processes on the initial coherent state of the driving field, we analyze its phase space dynamics within a cycle of the field and along the duration of the driving pulse envelope, and we show how the key action of conditioning on HHG and ATI processes can naturally lead to the generation of coherent-state superpositions of arbitrary high-photon number. We also discuss how the laser-atom interaction conditions, in experiment, can be used to control the quantum features of these states. The theoretical results have been confirmed experimentally by showing the dependence of the nonclassical features of the generated light after HHG on the atomic gas pressure. Furthermore, to demonstrate the high-photon nature of the generated cat states, we have experimentally achieved a nine-photon number optical Schrödinger cat state.

The paper is organized as follows. In Sec. II A we present the Schrödinger equation governing the interaction between the atom and the quantized field, and in Secs. II B and II C we condition the obtained equation to the HHG and ATI processes and study the obtained quantum optical states. In Sec. III A we describe the experimental setup that allows for the conditioning onto HHG, which is later used in Sec. III B to show the transition from a “cat” state to a “kitten” by changing the atomic density in the interaction region, and in Sec. III C to show the high-photon-number nature of the obtained quantum optical cat states. In the present work, we consider as low- and high-photon-number states those states having mean photon number $\langle n \rangle$ in the range $\langle n \rangle \leq 2$ and $\langle n \rangle > 5$, respectively. Finally, in Sec. IV we provide a discussion on the perspective toward future implications of this work.

II. THEORY

A. Theoretical background

The qualitative understanding of the interaction is traditionally provided by the well-known three-step model [21,22,24]. According to this model, when a low-frequency [usually in the infrared (IR) spectral range] intense linearly polarized laser field interacts with an atom or molecule, an electron tunnels out from the considered system, then it accelerates in the continuum gaining energy from the laser field, and, within the same cycle of the field, it may recollide elastically or inelastically with the parent ion. This process is repeated every half-cycle of the laser field leading to the generation of ions, photoelectrons, or photons with frequencies higher than the driving laser field [high harmonics (HH)]. The non-recolliding electrons and the electrons that recollide elastically with the parent ion contribute to the generation of above-threshold ionization photoelectrons [31,51], while the

inelastic recollision leads to the generation of HH (the electron recombines with the ion emitting a photon) or multiple charged ions (for example, via nonsequential double ionization) [31].

Our fully quantized theoretical approach relies on the study of the reduction of the amplitude ($\delta\alpha_L$) in the initial coherent state of the fundamental mode ($|\alpha_L\rangle$) as a consequence of its interaction with the atomic ensemble. The performance of further quantum operations, which we shall refer to hereafter as *conditionings*, allows us to constrain our equations to specific strong-field physics processes, in particular to HHG and ATI. As a consequence of these operations, schematically illustrated in Fig. 1, the outgoing final state of the fundamental mode is given as the superposition of amplitude-shifted coherent states, as was shown in [50] for the HHG scenario.

Briefly (further details about the calculations can be found in Appendix A), we start from the time-dependent Schrödinger equation (TDSE) describing the interaction of the quantized field with the considered atom within a single active electron picture and in the dipole approximation. After performing a set of unitary transformations, it can be shown that the final TDSE characterizing the joint state between the electron and the field modes is given by

$$i\hbar \frac{\partial}{\partial t} |\psi(t)\rangle = -e\hat{\mathbf{E}}_Q(t) \cdot \hat{\mathbf{R}}_H(t) |\psi(t)\rangle, \quad (1)$$

where $e\hat{\mathbf{R}}_H(t)$ is the time-dependent dipole operator in the so-called semiclassical interaction picture (see Appendix A) acting exclusively on the electronic degrees of freedom, and $\hat{\mathbf{E}}_Q(t)$ is a discrete version the electric field operator acting on the fundamental modes and its harmonics up to the cutoff region of the spectrum, that is,

$$\hat{\mathbf{E}}_Q(t) = -i\hbar \mathbf{g}(\omega_L) f(t) \left[(\hat{a}^\dagger - \hat{a}) + \sum_{q=2}^{\text{cutoff}} \sqrt{q} (\hat{b}_q^\dagger - \hat{b}_q) \right], \quad (2)$$

where \hat{a} (\hat{a}^\dagger) and \hat{b}_q (\hat{b}_q^\dagger) are the annihilation (creation) operators acting on the fundamental and q th harmonic, respectively, $\mathbf{g}(\omega_L) \propto \sqrt{\omega_L/V_{\text{eff}}}$ is the coefficient that enters into the expansion of the laser electric modes and that depends on V_{eff} , which is the effective quantization volume [5,52], and $0 \leq f(t) \leq 1$ is a dimensionless function describing the pulse envelope.

Note that, as a consequence of the intense laser-atom interaction, we can either find the electron remaining in the ground state or in a continuum state. In the following, we show how Eq. (1) can be used for the quantum optical description of two of the most central processes in strong-field physics: HHG and ATI.

B. Quantum optical dynamics of HHG

In the HHG process, first the electron gets transferred to the continuum via tunneling ionization due to the strong laser field we are applying, and later it recombines with the parent ion that was left behind, ending up again in the ground state of the system. Therefore, in order to get information about the HHG photonic quantum state, we condition Eq. (1) onto the atomic ground state $|g\rangle$, i.e.,

$$i\hbar \frac{\partial}{\partial t} \langle g | \psi(t) \rangle = -\hat{\mathbf{E}}_Q(t) \cdot \langle g | e\hat{\mathbf{R}}_H(t) | \psi(t) \rangle. \quad (3)$$

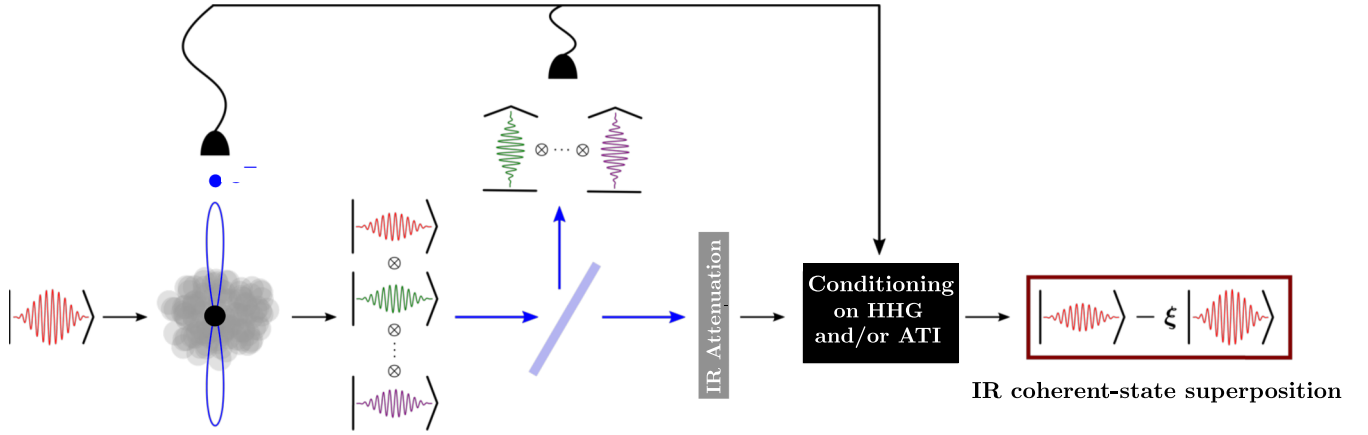


FIG. 1. Scheme of the different *conditionings*. A high-photon-number coherent state coming from a laser source interacts with an atomic gas jet. As a consequence of the strong-field interaction that takes place, some electrons will ionize and, subsequently, may either recombine with the parent ion generating high-order harmonics or stay in the continuum. Thus, depending on the particular process we want to consider, we can look at the generated harmonics in case we want to study the quantum optical state of light obtained after HHG, and/or we can measure the generated photoelectrons in order to include ATI processes. We can further constrain this last measurement to photoelectrons that have a specific kinetic momentum, or consider all possible momenta. As a consequence of these conditioning measurements, the final quantum optical state of the IR mode can be written as a superposition of two or more coherent states.

After strong-field physics approximations, the above equation can be expressed as (see Appendix B)

$$i\hbar \frac{\partial}{\partial t} |\Phi(t)\rangle = -\hat{\mathbf{E}}_Q(t) \cdot \mathbf{d}_H(t) |\Phi(t)\rangle, \quad (4)$$

where $|\Phi(t)\rangle = \langle \mathbf{g} | \psi(t) \rangle$ and $\mathbf{d}_H(t) = \langle \mathbf{g} | e^{\hat{\mathbf{R}}_H(t)} | \mathbf{g} \rangle$ is the averaged time-dependent dipole operator. Here, $\mathbf{d}_H(t)$ can be easily computed by numerically solving the TDSE, or by means of the strong-field approximation (SFA) theory [22,23,53]. Whatever the method used, this equation can be easily solved as it is written as a linear combination of photon creation and annihilation operators for the different modes considered in the problem. This has a natural implication, namely that the final solution is given by a product state of all the modes participating in the process,

$$|\Phi(t)\rangle = e^{i\varphi_L(t)} |\alpha_L + \delta\alpha_L e^{-i\omega_L t}\rangle \otimes e^{i\varphi_2(t)} |\beta_2 e^{-i2\omega_L t}\rangle \otimes \dots \otimes e^{i\varphi_q(t)} |\beta_q e^{-iq\omega_L t}\rangle \otimes \dots, \quad (5)$$

where $\delta\alpha_L(t)$ and $\beta_q(t)$ are defined as

$$\delta\alpha_L(t) = N \mathbf{g}(\omega_L) \cdot \int_{t_0}^t d\tau f(\tau) \mathbf{d}_H(\tau) e^{i\omega_L \tau}, \quad (6)$$

$$\beta_q(t) = N \sqrt{q} \mathbf{g}(\omega_L) \cdot \int_{t_0}^t d\tau f(\tau) \mathbf{d}_H(\tau) e^{iq\omega_L \tau}. \quad (7)$$

We recall that our analysis has been performed within the single active electron picture. However, in Eqs. (6) and (7) we have assumed that we have N atoms that contribute to the HHG process coherently in a phase-matched way. One can see (see Appendix B) that the shift $\delta\alpha_L(t)$ onto the initial coherent state is related to the electron and ionization processes taking place in HHG, while the β_q 's recover their features regarding the harmonic emission.

To study the backaction of the electron acceleration over the initial state of the system, we investigate the phase space dynamics of $\delta\alpha_L$ using the mean value of the photonic quadratures \hat{x}_L and \hat{p}_L . Furthermore, we consider the interaction of

the laser pulse with a single atom, so that $\delta\alpha_L$ is determined by Eq. (6) when $N = 1$. Defining \hat{x}_L, \hat{p}_L as

$$\hat{x}_L = \frac{1}{\sqrt{2}} (\hat{a} + \hat{a}^\dagger) \quad \text{and} \quad \hat{p}_L = \frac{1}{i\sqrt{2}} (\hat{a} - \hat{a}^\dagger), \quad (8)$$

it can be shown that their mean values with respect to Eq. (5) are

$$\begin{aligned} \langle \hat{x}_L(t) \rangle &= \sqrt{2} |\alpha_L + \delta\alpha_L(t)| \cos(\omega_L t + \theta(t)), \\ \langle \hat{p}_L(t) \rangle &= -\sqrt{2} |\alpha_L + \delta\alpha_L(t)| \sin(\omega_L t + \theta(t)), \end{aligned} \quad (9)$$

with $\theta(t)$ the phase factor of $[\alpha_L + \delta\alpha_L(t)] = |\alpha_L + \delta\alpha_L| e^{-i\theta(t)}$. The integral defining $\delta\alpha_L(t)$ was calculated numerically employing $\mathbf{d}_H(t)$ extracted from the QPROP software [54], using a sinusoidal squared laser pulse envelope with 12 cycles and fundamental wavelength $\lambda_L = 800$ nm. Figure 2(a) shows the amplitude shift of the coherent state in phase space, while Fig. 2(b) shows the time dependence of the amplitude $|\alpha_L + \delta\alpha_L|$ and the phase factor $\theta(t)$ [inset in Fig. 2(b)].

The dynamics of $\delta\alpha_L$ is summarized in the following four main features: (i) during the acceleration process, the ionized electron absorbs photons resulting in an enhancement of $|\delta\alpha_L|$, i.e., a reduction of $|\alpha_L + \delta\alpha_L|$ [see Fig. 2(b), and for more information see Appendix C]; (ii) $|\delta\alpha_L|$ increases with the amplitude of the driving field as the electron gains more kinetic energy; (iii) $|\delta\alpha_L|$ continuously increases during the laser pulse (having a maximum enhancement rate at the peak of the pulse envelope, where the field amplitude is maximum), reaching its maximum value at the end of the pulse; (iv) the $|\delta\alpha_L|$ enhancement rate follows the gradient of the driving electric field amplitude. This leads to an oscillatory modulation of frequency $2\omega_L$ of the enhancement of $|\delta\alpha_L|$ during the laser pulse. It is noted that an oscillatory modulation of frequency $2\omega_L$ has also been observed on the phase $\theta(t)$ [see the inset of Fig. 2(b)]. However, because this phase shift is in the order of 10^{-3} rad, its influence on the state of the field is considered negligible and thus it is not further discussed here.

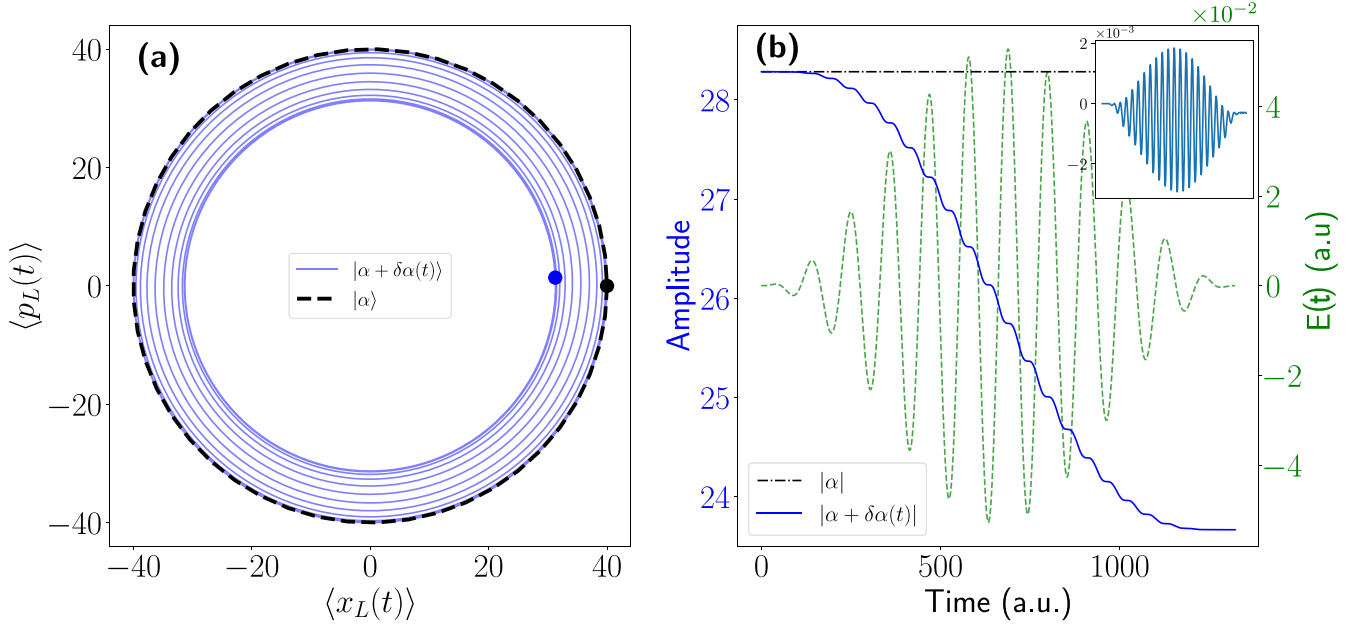


FIG. 2. Dynamics of the coherent shifted state obtained after HHG. (a) Dynamics of $|\alpha_L\rangle$ with $|\alpha_L| \approx 28$ (black dashed curve) and $|\alpha_L + \delta\alpha_L(t)\rangle$ (blue continuous curve) in phase space. The analysis was performed using $\mathbf{g}(\omega_L) \approx 10^{-1}$. The circles in the black dashed and blue continuous curves, which represent $|\alpha_L\rangle$ and $|\alpha_L + \delta\alpha_L(t)\rangle$, respectively, depict the final coherent-state amplitude obtained after the evolution. (b) Dependence of $|\alpha_L + \delta\alpha_L(t)|$ (blue continuous curve) on time. The black dashed line depicts the initial value of $|\alpha_L|$. The applied electric field is plotted with the dashed green line in atomic units (a.u.). The inset represents the dependence of the phase θ with time. We note that in this figure the values of α_L have been chosen in such a way that the effects of $\delta\alpha_L$ could be distinguished. In general, HHG processes take place with values of $|\alpha_L| \approx 10^6$.

Finally, we discuss how the aforementioned results can be used for the creation of optical Schrödinger cat states in the IR spectral region. We note that, although the above analysis is applicable for high-photon-numbers, in the following we discuss the case of low-photon-numbers states. This is because we are interested in providing results that can be used by an experiment that utilizes the quantum tomography (QT) method [55,56] for the quantum state characterization.

To create the coherent-state superposition between the initial coherent state of the field and its amplitude-shifted version, we condition the state of the fundamental field such that it corresponds to the one obtained after HHG as described in Ref. [50] (see also Appendix D). After reducing the amplitude of the fundamental laser mode, the key action for creating the nonclassical light state is the postselection of the coherent shifted state over those interaction events that lead to the generation of at least one harmonic photon. This is done by performing an anticorrelated measurement between the signal obtained from the harmonic emission and the depletion obtained in the fundamental mode [50,57]. This operation, which we refer to as *conditioning on HHG*, is mathematically expressed for high values of the harmonic cutoff via the projector operator [58]

$$P = \mathbb{1} - |\alpha_L\rangle\langle\alpha_L|. \quad (10)$$

When this operator acts over Eq. (5), and after conditioning the harmonics to be found in $\bigotimes_{q=2}^{\text{cutoff}} |\beta_q\rangle$, the final state of the system is given (up to normalization) by

$$|\Phi_{\text{HHG}}\rangle = |\alpha_L + \delta\alpha_L\rangle - \xi|\alpha_L\rangle, \quad (11)$$

which is the superposition of two coherent states, commonly referred to as optical cat states [59,60], where $\xi \approx \langle\alpha_L|\alpha_L + \delta\alpha_L\rangle$. Note that the dependence of the weight ξ with $\delta\alpha_L$ allows us to control the quantum features of the state [61], for example by modifying the density of atoms in the interaction region or the intensity of the employed laser field. In particular, in the limit where $\delta\alpha_L \rightarrow 0$ we get an optical “kitten” state characterized by $|\Phi_{\text{HHG}}\rangle \approx D(\alpha_L)|1\rangle$ (see Appendix D), while the limit $0 < \xi < 1$ leads us to the “genuine cat” state presented in Eq. (11). Furthermore, if $|\delta\alpha_L|$ becomes a very large quantity such that $\xi \rightarrow 0$, then the final state is just given by the amplitude-shifted coherent state $|\Phi_{\text{HHG}}\rangle = |\alpha_L + \delta\alpha_L\rangle$.

The different cases discussed above are shown in Fig. 3, where the Wigner function of the final state (see Appendix D) has been calculated using an electric field with a sinusoidal squared envelope, 12 cycles of duration (~ 30 fs duration), wavelength $\lambda_L = 800$ nm, and amplitude $E_L = 0.053$ a.u., where a.u. denotes atomic units (which corresponds to a laser intensity of about 10^{14} W/cm²). At the beginning of the pulse [Figs. 3(a) and 3(b)], where the driving field amplitude is small, $\delta\alpha_L$ is small, resulting in the creation of a “kitten” state, while at the end of the pulse, where $\delta\alpha_L$ is getting larger [according to Fig. 2(b)], the Wigner function depicts a genuine “cat” state [Figs. 3(e)–3(f)]. Evidently, in the case of reducing the intensity of the driving field, the final state would be a “kitten.”

One of the main advantages of using the Wigner function as an observable for the final quantum optical state of the field is that it allows the superposition between the two

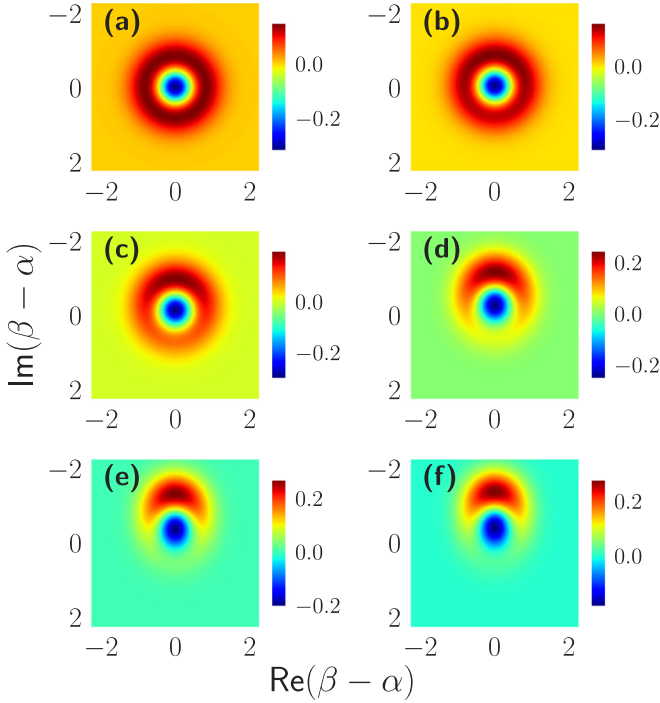


FIG. 3. Wigner function evolution along the pulse when conditioning to HHG. Here, we have used the same electric field as in Fig. 2, and we see how the Wigner function looked after (a) 2, (b) 4, (c) 6, (d) 8, (e) 10, and (f) 12 cycles. $\text{Re}[\beta - \alpha] \equiv x_L$, $\text{Im}[\beta - \alpha] \equiv p_L$, with x_L and p_L the values of the quadrature field operators $\hat{x}_L = (\hat{a} + \hat{a}^\dagger)/\sqrt{2}$ and $\hat{p}_L = (\hat{a} - \hat{a}^\dagger)/i\sqrt{2}$, respectively.

coherent states to be seen explicitly. If the depletion in the fundamental is small enough to witness a Wigner negativity, the anticorrelation measurement is not able to exactly distinguish the contributions from the depleted field $|\alpha_L + \delta\alpha_L\rangle$ and the input state $|\alpha_L\rangle$. It is the indistinguishability at the detector that leads to the observed interference. In particular, if $\delta\alpha_L$ is too small, we get the “kitten” case where both states contribute equally to the Wigner function, and the distribution has a homogeneous ringlike shape structure around a negativity center that witnesses the quantum superposition. As the depletion increases, we get a genuine “cat” for which the distribution is not homogeneous, since the contribution of $|\alpha_L + \delta\alpha_L\rangle$ is bigger than the one provided by $|\alpha_L\rangle$ because of the ξ prefactor. This increasing in the distinguishability leads to smaller values of the Wigner negativity. Finally, in the case of enormous values of the depletion (leading to $\xi \rightarrow 0$), we only observe the contribution from $|\alpha_L + \delta\alpha_L\rangle$, and hence the Wigner function is a Gaussian centered around $\alpha_L + \delta\alpha_L$.

C. Quantum optical dynamics of ATI

As mentioned above, ATI processes occur when the ionized electron does not re-collide with the parent ion, or if it does, the process takes place elastically. Therefore, to study these phenomena within our formalism, we will condition Eq. (1) upon finding the electron in continuum states, which we will simply represent as $|\mathbf{v}\rangle$, where \mathbf{v} denotes the outgoing kinetic momenta of the electron. In this case, the conditioned

Schrödinger equation reads

$$i\hbar \frac{\partial}{\partial t} \langle \mathbf{v} | \psi(t) \rangle = -\hat{\mathbf{E}}_Q(t) \cdot \langle \mathbf{v} | \mathbf{e} \hat{\mathbf{R}}_H(t) | \psi(t) \rangle. \quad (12)$$

At this point, we introduce the SFA theory assumptions [22] and neglect the effects of the electronic bound excited states. Thus, introducing the SFA version of the identity

$$\mathbb{1} \approx |\mathbf{g}\rangle \langle \mathbf{g}| + \int d\mathbf{v} |\mathbf{v}\rangle \langle \mathbf{v}| \quad (13)$$

in Eqs. (3) and (12), we get the following set of coupled differential equations:

$$\begin{aligned} i\hbar \frac{\partial}{\partial t} |\Phi(t)\rangle &= -\hat{\mathbf{E}}_Q(t) \cdot \mathbf{d}_H(t) |\Phi(t)\rangle \\ &\quad - \int d\mathbf{v} \hat{\mathbf{E}}_Q(t) \cdot \mathbf{d}_H(\mathbf{v}, t) |\Phi(\mathbf{v}, t)\rangle, \\ i\hbar \frac{\partial}{\partial t} |\Phi(\mathbf{v}, t)\rangle &= -\hat{\mathbf{E}}_Q(t) \cdot \mathbf{d}_H^*(\mathbf{v}, t) |\Phi(t)\rangle \\ &\quad - \int d\mathbf{v}' \hat{\mathbf{E}}_Q(t) \cdot \mathbf{d}_H(\mathbf{v}, \mathbf{v}', t) |\Phi(\mathbf{v}', t)\rangle, \end{aligned} \quad (14)$$

where we denote the state conditioned to ATI as $|\Phi(\mathbf{v}, t)\rangle = \langle \mathbf{v} | \psi(t) \rangle$, $\mathbf{d}_H(\mathbf{v}, t) = \langle \mathbf{v} | \mathbf{e} \hat{\mathbf{R}}_H(t) | \mathbf{g} \rangle$ is the time-dependent dipole moment matrix element between states $|\mathbf{v}\rangle$ and $|\mathbf{g}\rangle$, and $\mathbf{d}_H(\mathbf{v}, \mathbf{v}', t) = \langle \mathbf{v} | \mathbf{e} \hat{\mathbf{R}}_H(t) | \mathbf{v}' \rangle$ represents the time-dependent dipole moment matrix element between states $|\mathbf{v}\rangle$ and $|\mathbf{v}'\rangle$.

In the spirit of the SFA theory, we may neglect the effect of the continuum-continuum transitions and obtain the contribution to ATI corresponding to direct tunneling, or treat the continuum-continuum transitions perturbatively [62–65] in order to describe the rescattered ATI electrons at higher energies up to $10U_p$, where U_p is the ponderomotive potential defined as $U_p = e^2 E^2 / 4m\omega_L^2$, with E the electric field amplitude, and m and e the electron’s mass and charge, respectively. Thus, considering electrons of “low” kinetic energy ($< 2U_p$) and keeping the strong-field approximations, the state conditioned to ATI reads

$$|\Phi(\mathbf{v}, t)\rangle = \frac{i}{\hbar} \int_{t_0}^t dt' \hat{\mathbf{E}}_Q(t') \cdot \mathbf{d}_H^*(\mathbf{v}, t') |\Phi(t')\rangle, \quad (15)$$

where $|\Phi(t)\rangle$ is the solution to Eq. (3).

To derive the reduced density matrix for the electromagnetic field that corresponds to ATI processes, we will consider two different strategies: (i) we condition on ATI electrons that have a specific outgoing direction and kinetic momentum \mathbf{v} , which leads to a reduced density matrix of the form $\rho = |\Phi(\mathbf{v}, t)\rangle \langle \Phi(\mathbf{v}, t)|$ (pure state); (ii) we condition on all possible ATI electrons without distinguishing on the particular direction and kinetic momentum of the outgoing electrons, which leads to $\rho = \int d^3v |\Phi(\mathbf{v}, t)\rangle \langle \Phi(\mathbf{v}, t)|$ (mixed state).

For the first scenario, assuming that during the ATI process the harmonic coherent-state amplitudes $[\beta_q$ in Eq. (5)] stay very close to the vacuum, one can see that the final state of the system can be written as (for more details, see Appendix E)

$$\begin{aligned} |\tilde{\Phi}(\mathbf{v}, t)\rangle &\approx \frac{i}{\hbar} \sum_{j=0}^{N-1} \int_{t_j}^{t_{j+1}} dt' \hat{\mathbf{E}}_L(t') \cdot \mathbf{d}_H^*(\mathbf{v}, t') \\ &\quad \times |(j+1)\Delta\rangle, \end{aligned} \quad (16)$$

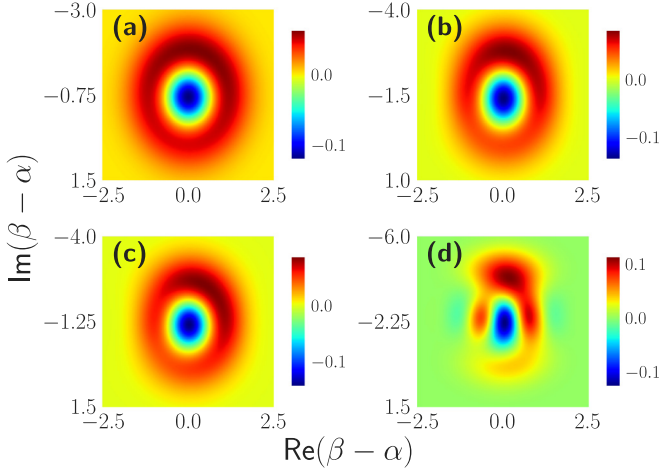


FIG. 4. Wigner function after single-ionization ATI. Dependence of the Wigner function with the number of half-cycles \mathcal{N} of equal intensity provided by a laser source, and with the shift between two consecutive coherent states Δ . In these subplots, we consider (a) $\mathcal{N} = 5$, $\Delta = -0.25i$; (b) $\mathcal{N} = 5$, $\Delta = -0.5i$; (c) $\mathcal{N} = 8$, $\Delta = -0.25i$; (d) $\mathcal{N} = 8$, $\Delta = -0.5i$. $\text{Re}[\beta - \alpha] \equiv x_L$, $\text{Im}[\beta - \alpha] \equiv p_L$, with x_L and p_L the values of the quadrature field operators $\hat{x}_L = (\hat{a} + \hat{a}^\dagger)/\sqrt{2}$ and $\hat{p}_L = (\hat{a} - \hat{a}^\dagger)/i\sqrt{2}$, respectively.

where \mathcal{N} is the number of half-cycles and Δ is the amount of photons absorbed in each half-cycle (as discussed in Fig. 2). We see that the final state is given as a superposition of different coherent states (which, in principle, is larger than two), where each of them is affected by the instantaneous value of the electric field operator evaluated at time t' . In Fig. 4, we present the Wigner functions calculated from Eq. (16). In these calculations, we assumed that the electron tunnels out with zero kinetic energy, and we considered (a) $\mathcal{N} = 5$, $\Delta = -0.25i$, (b) $\mathcal{N} = 5$, $\Delta = -0.5i$, (c) $\mathcal{N} = 8$, $\Delta = -0.25i$, and (d) $\mathcal{N} = 8$, $\Delta = -0.5i$. As we can see, as both \mathcal{N} and Δ increase, the distance between the two outermost coherent states appearing in the superposition also increases and we switch from a kitten state [like the one in Fig. 4(a)] to more complicated coherent-state superpositions [like the one in Fig. 4(d)]. Note that the distribution shown in Fig. 4(d) differs from the symmetric one coming from a coherent-state superposition of the form $|\alpha\rangle \pm |-\alpha\rangle$ in that we have more states in the superposition that are contributing as well to the Wigner function.

Another difference that we observe in these plots is that some of the Wigner distributions obtained for single-ionization ATI depict a small rotation [see, for instance, Fig. 4(c)]. This is related to a change in the phase of the coherent states appearing in the superposition. However, it may also be the case that small rotations are related to a change in the phase of the respective amplitudes in the superposition, which in the end is related to how we are implementing the conditioning operations. In HHG, the coefficient ξ appears as a consequence of the conditioning measurement that is being applied to the optical modes, and if both $\delta\alpha$ and α have either the same phase or a phase difference of π , as happens in the present manuscript, then ξ is a real quantity. In ATI, the coefficients weighting the superposition have a

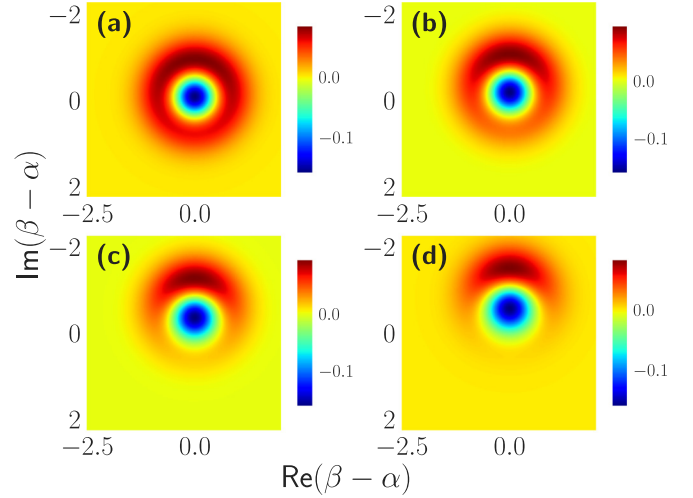


FIG. 5. Wigner function after ATI and conditioning over all possible momenta. Calculated Wigner functions after considering equal and time-independent coherent shifts (a) $\delta\alpha = -0.1i$, (b) $\delta\alpha = -0.25i$, (c) $\delta\alpha = -0.5i$, and (d) $\delta\alpha = -0.75i$. For the computation of the Wigner function, we have further considered some approximations over the time-dependent integrals, which are detailed in Appendix E. $\text{Re}[\beta - \alpha] \equiv x_L$, $\text{Im}[\beta - \alpha] \equiv p_L$, with x_L and p_L the values of the quadrature field operators $\hat{x}_L = (\hat{a} + \hat{a}^\dagger)/\sqrt{2}$ and $\hat{p}_L = (\hat{a} - \hat{a}^\dagger)/i\sqrt{2}$, respectively.

different nature, as they depend, via $\mathbf{d}^*(\mathbf{v}, t)$, on the electron's trajectory before being detected, which in general is a complex quantity. Thus, in single-ionization ATI we might find changes in the coefficients from one term to the other, leading to these rotations. Related to this, we expect that one of the main effects of the carrier-envelope phase, i.e., the change of phase between the carrier wave and the field envelope, over the final Wigner distribution is the presence of these rotations, which would affect the HHG state. However, further research has to be done in this direction, since our analysis is restricted to a multicycle pulse.

For the second scenario, in order to gain intuition about the obtained mixed state, we are going to consider a linearly polarized field, and assume (i) that during the ATI process the harmonic coherent-state amplitudes stay very close to the vacuum, and (ii) that the generated coherent shifts are identical and time-independent. In general this is not true and, as discussed in Fig. 2(b), the IR coherent state is continuously increasing (in modulus) along the pulse. However, for single-electron ionization processes, one may expect this shift to remain very small. Therefore, under these considerations the ATI state conditioned to all outgoing momenta reads

$$\rho_{\text{ATI-IR}} = \int_{t_0}^t dt' \int_{t_0}^t dt'' \hat{E}_L(t') |\delta\alpha\rangle \langle \delta\alpha| \hat{E}_L(t'') \times K(t', t'') e^{i\varphi(t')} e^{-i\varphi(t'')}, \quad (17)$$

where \hat{E}_L is the part of the electric field operator in Eq. (2) that acts over the fundamental mode and $K(t, t'') = \langle \hat{d}_H(t') \hat{d}_H(t'') \rangle - \langle \hat{d}_H(t') \rangle \langle \hat{d}_H(t'') \rangle$ (see Appendix E). The results for the calculated Wigner functions are shown in Fig. 5, where in each of the subplots we have considered increasing

values of $\delta\alpha$ [from (a) to (d)]. We note that its shape is very similar to a “cat” state, and, as it happens in HHG, as $\delta\alpha$ increases it tends to a typical Gaussian state. This is due to the approximations we considered and that lead to Eq. (17), since in the limit when $\delta\alpha$ is very big we can write $\hat{E}_L(t)|\delta\alpha\rangle \propto |\delta\alpha\rangle$, which leads to the Gaussian-like Wigner function. However, we note that this limit is not compatible with our assumptions, since we expect $\delta\alpha$ to be small in the single active electron picture. More nonclassical features are expected for the exact state obtained after the interaction, i.e., without approximations, due to the change of $\delta\alpha$ in time. We also note that the rotations obtained in the Wigner distributions appearing in *single-ionization ATI* do not show up in this case. Although this is an expected feature given that the $K(t, t')$ is a complex function, the approximations we consider here in order to gain intuition about the shape of the final Wigner functions do not take this feature into account.

Finally, we remark that the plots we have presented thus far for the ATI process correspond to the state right after the interaction, i.e., in the displaced frame of reference. However, for the Wigner function characterization this is not a problem as, by implementing them, one observes the same features as the ones shown in our figures upon a shift and a rotation.

III. EXPERIMENTAL RESULTS

A. Experimental setup

The quantum features of the nonclassical light state of the fundamental mode exiting the atomic medium depend on the conditioning approaches used (HHG and/or ATI) and on $\delta\alpha_L$, which introduces the dependence with the gas pressure in the interaction area [Eq. (6)]. Here, the action of conditioning was achieved using the quantum spectrometer (QS) approach [57,66], and the quantum state characterization was performed by means of homodyne detection and the well-known QT method [55,56]. In the following, after the description of the operation principle of the experimental approach (see also Ref. [50] and Appendix F), we experimentally demonstrate the dependence of the coherent-state superposition (created by conditioning on HHG) on $\delta\alpha_L$, and the generation of high-photon-number optical “cat” states. Following a similar strategy, the method can be used for the characterization of optical coherent-state superpositions generated by conditioning on the ATI process (see Appendixes E and G). This can be achieved by using the ATI photoelectron signal recorded by means of a time-of-flight electron spectrometer (see Appendix G, Fig. 10).

A schematic of the experimental approach is shown in Fig. 6. The experiment was performed using as a primary laser source a Ti:sapphire laser system delivering linearly polarized ≈ 35 fs pulses of $\lambda \approx 800$ nm carrier wavelength. The IR laser beam was separated into the branches of an interferometer by a beam separator BS_1 . The reflected IR beam serves as a reference beam of the QT method. The transmitted IR beam was focused with an intensity $\approx 8 \times 10^{13}$ W/cm² into a xenon pulsed gas jet, where harmonics up to 21st order have been generated. The photon number of the generated XUV beam (reflected by a harmonic separator HS) and the photon number of a portion the IR beam (reflected by an IR beam separator

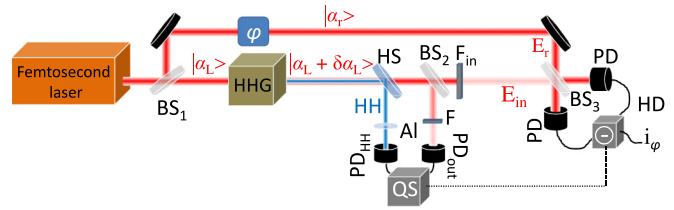


FIG. 6. Simplified scheme of the experimental setup. $|\alpha_L\rangle$ and $|\alpha_r\rangle$ are the IR coherent states transmitted and reflected by an IR beam separator BS_1 . The transmitted IR beam is focused into a xenon gas jet where the high harmonics (HH) are generated. $|\alpha_L + \delta\alpha_L\rangle$ is the state of the IR field after the interaction. HS is a harmonic separator that reflects the HH and leaves the IR beam to pass through. $BS_{2,3}$ is an IR beam separator and splitter, respectively. PD_{out} and PD_{HH} are the IR and HH photodetectors, respectively, used by the QS to condition the IR field exiting the atomic medium on the HHG. Just before PD_{HH} , a 150-nm-thick aluminum filter was placed in order to select the harmonics with $q \geq 11$ and block any residual part of the IR beam. F and F_{in} are neutral density filters. E_{in} is the state of the IR field to be characterized. PD are the IR photodetectors used by the balanced detector of the homodyne detection (HD) system. E_r is the field of the reference beam. φ is the controllable phase shift introduced in the reference beam, and i_φ is the photocurrent difference, which is proportional to the measurement of \hat{x}_φ . When the xenon gas jet and the QS are switched on, the homodyne detection system provides the measurement \hat{x}_φ only when the IR field exiting the atomic medium is conditioned on, and the HHG via QT provides the Wigner function of the light state $|\Phi_{post}\rangle = |\alpha_L + \delta\alpha_L\rangle - \xi|\alpha_L\rangle$ with $\xi = \langle\alpha_L|\alpha_L + \delta\alpha_L\rangle$.

BS_2) have been recorded for each laser shot by the PD_{HH} and PD_{out} photodetectors, respectively. These were used by the QS to condition the IR field exiting the atomic medium on the HHG process (see Appendix F). After BS_2 , the mean photon number of the IR field was reduced (by means of neutral density filters F_{in}) to the level of a few photons per pulse. The IR field amplitude before reaching the balanced detector of the homodyne detection system is denoted by E_{in} . The E_{in} field was spatiotemporally overlapped in a beam splitter (BS_3) with the high-photon-number reference field E_r coming from the second branch of the interferometer. The interfering fields after BS_3 were recorded by a balanced detector, which provides at each value of φ for each laser shot the photocurrent difference i_φ . The values of i_φ are directly proportional to the measurement of the electric field operator $\hat{E}_{in}(\varphi) \propto \hat{x}_\varphi = \cos(\varphi)\hat{x} + \sin(\varphi)\hat{p}$, and they have been used for the reconstruction of the Wigner function [55,56,67] (see Appendixes G and H). When the xenon gas jet and the QS were switched on, the homodyne detection system measures the \hat{x}_φ only when the IR field exiting the atomic medium is conditioned on the HHG, providing via QT the Wigner function of the light state $|\Phi_{post}\rangle = |\alpha_L + \delta\alpha_L\rangle - \xi|\alpha_L\rangle$ with $\xi = \langle\alpha_L|\alpha_L + \delta\alpha_L\rangle$.

B. Dependence of the coherent-state superposition on $\delta\alpha_L$: Optical “kitten” and “cat” states

To show the dependence of the quantum features of the coherent-state superposition with $\delta\alpha_L$, we have measured the Wigner function $W(x, p)$ for two different values of $\delta\alpha_L$ when

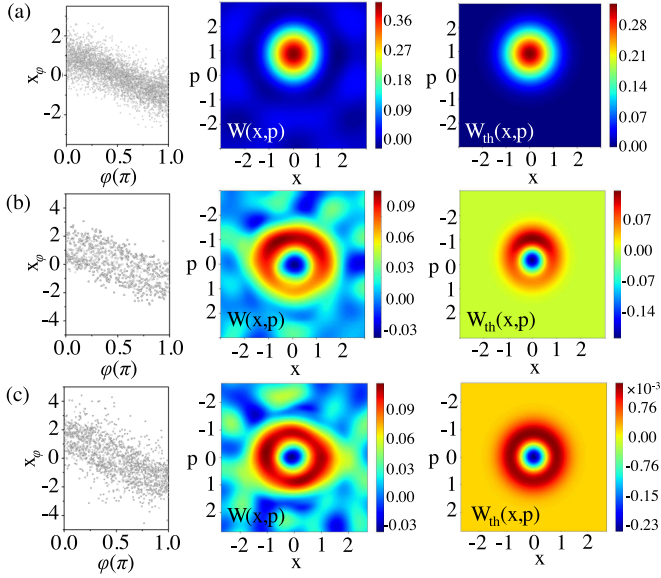


FIG. 7. Optical “cat” and “kitten” states created by conditioning on HHG for different values of $|\delta\alpha_L|$. The left, middle, and right panels show the measured \hat{x}_φ , the corresponding reconstructed $W(x, p)$, and the theoretically calculated $W_{\text{th}}(x, p)$, respectively, projected onto the (x, p) plane. (a) Coherent state of driving laser field measured when the Xe gas and QS approach were switched off. (b) Optical “cat” state measured when the Xe gas jet and the QS were switched on and the harmonic yield was close to maximum. The corresponding $W_{\text{th}}(x, p)$ has been calculated for $|\delta\alpha_L| \approx 0.5$, where $|\alpha_L| \approx 1.4$ and $|\xi| \approx 0.88$. (c) Optical “kitten” state measured when the harmonic yield was reduced by a factor of ≈ 25 , i.e., $\delta\alpha_L$ by a factor of ≈ 5 , compared to the harmonic yield of (b). The corresponding $W_{\text{th}}(x, p)$ has been calculated for $|\delta\alpha_L| \approx 0.1$, where $|\alpha_L| \approx 1.3$ and $|\xi| \approx 0.99$. x and p are the values of the quadrature field operators $\hat{x} = (\hat{a} + \hat{a}^\dagger)/\sqrt{2}$ and $\hat{p} = (\hat{a} - \hat{a}^\dagger)/i\sqrt{2}$. The Wigner functions in these plots have been centered around the value of α_L .

we condition on HHG. This is shown in Fig. 7 together with the measurement of the coherent state of the driving field [Fig. 7(a)]. The left panels show the measured \hat{x}_φ , the middle panels the corresponding reconstructed $W(x, p)$, and the right panels the theoretically calculated $W_{\text{th}}(x, p)$. As $\delta\alpha_L \propto N$ [Eq. (6)], the change of $\delta\alpha_L$ was achieved by varying the number of atoms N in the interaction region (using the delay between the laser pulse arrival and the opening of the Xe gas nozzle). It is noted that for experimental reasons (gas load in the vacuum chamber), in the present experiment the maximum value of the used N was set such that the harmonic signal was slightly lower (a factor of ≈ 2) than its maximum value. Since the harmonic yield (Y) is $Y \propto N^2$, we then get $\delta\alpha_L \propto Y^{1/2}$. This relation provides a useful experimental guide for controlling the value of $\delta\alpha_L$ by monitoring the integrated signal of the harmonics passing through the aluminum filter.

For reasons of completeness and for evaluating the performance of the experimental setup, it is useful to measure first the coherent state of the driving field by switching off the Xe gas jet and the QS. This is shown in Fig. 7(a). As expected, the state of the IR driving field is coherent, depicting a $W(x, p)$ with a Gaussian distribution. The same result was obtained when the Xe gas and the QS were switched on and off, re-

spectively. By switching on both the Xe gas jet (at conditions where the harmonic generation yield is close to maximum) and the QS, as reported in Ref. [50], an optical “cat” state with mean photon number $\langle n \rangle \approx 1.74 \pm 0.03$ has been recorded [Fig. 7(b)]. The $W(x, p)$ depicts a half-ring-like shape with a central negative minimum located at $(x_{\text{min}}, p_{\text{min}}) \approx (0, 0)$ and a maximum at $(x_{\text{max}}, p_{\text{max}}) \approx (0, -1)$, which is in agreement with the $W_{\text{th}}(x, p)$ obtained by the theoretical calculations for $|\delta\alpha_L|$ in the range of 0.4–0.5. In Fig. 7(b) we show the $W_{\text{th}}(x, p)$ for $|\delta\alpha_L| \approx 0.5$, where $|\alpha_L| \approx 1.4$ and $|\xi| \equiv |\langle \alpha_L + \delta\alpha_L | \alpha_L \rangle| \approx 0.88$. The value of $|\alpha_L|$ has been obtained by the equation $\langle n \rangle = \langle \Phi_{\text{post}} | \hat{n} | \Phi_{\text{post}} \rangle$ using as $\langle n \rangle$ the value of the measured mean photon number. When we reduce the Y by a factor of ≈ 25 , i.e., $\delta\alpha_L$ by a factor of ≈ 5 , the state superposition transitions from an optical “cat” to a “kitten” state. This is shown in Fig. 7(c), where an optical “kitten” state with $\langle n \rangle \approx 2.54 \pm 0.05$ has been recorded. In this case, the measured $W(x, p)$ depicts a full-ring shape with a central negative minimum located at $(x_{\text{min}}, p_{\text{min}}) \approx (0, 0)$. This is in agreement with the $W_{\text{th}}(x, p)$ obtained by the theoretical calculations obtained for $|\delta\alpha_L| \approx 0.1$, where $|\alpha_L| \approx 1.3$ and $|\xi| \approx 0.99$. We note that, for values of $|\delta\alpha_L| < 0.1$, our cat state behaves as a displaced Fock state, as there is no pronounced maximum on the ring-shaped phase space distribution.

C. Generation of high-photon-number optical “cat” states

For applications in quantum technology, it is also important to be able to increase the photon number of the produced optical “cat” states. As was mentioned before, the present approach can be used for the production of arbitrary high-photon-number “cat” states. To show this, we have recorded a nine-photon shifted optical “cat” state (Fig. 8) created by conditioning on HHG. Figure 8(a) shows the measurement of \hat{x}_φ used to reconstruct the Wigner function shown in phase space in Fig. 8(b). The measurement was performed using a value of N approximately close to the value used to record the low-photon-number optical “cat” state shown in Fig. 7(b), while the photon number has been increased by means of F_{in} (Fig. 6). This was achieved by the fine adjustment of the angle of the F_{in} filter with respect to the incoming beam. In this case, an optical “cat” state with $\langle n \rangle \approx 9.4 \pm 0.1$ has been recorded. The $W(x, p)$ depicts a half-ring-like shape with a central minimum located at $(x_{\text{min}}, p_{\text{min}}) \approx (0, -0.2)$ and a maximum at $(x_{\text{max}}, p_{\text{max}}) \approx (0, -1.2)$. The shape of the measured $W(x, p)$ is reasonably close to the Wigner function $[W_{\text{th}}(x, p)]$ obtained by the theoretical calculations for $|\delta\alpha_L|$ in the range of 0.6–1.1. In Fig. 8(c), we show the $W_{\text{th}}(x, p)$ for $|\delta\alpha_L| \approx 0.8$, where $|\alpha_L| \approx 3.7$ and $|\xi| \approx 0.73$. The lack of negative values at the position of the minimum of the measured $W(x, p)$ is attributed to limitations of the present experimental approach in obtaining the Wigner function and the photon number with accuracy better than ± 0.004 and $\approx 1.5\%$, respectively (see Appendixes G and H).

The limitations introduced for further increasing the mean photon number of the shifted optical cat state are associated with the resolution of the detection system and the decoherence effects (see Appendixes H and I, respectively), which cannot be excluded. A quantitative analysis of the decoherence effects and their dependence on the photon number of the

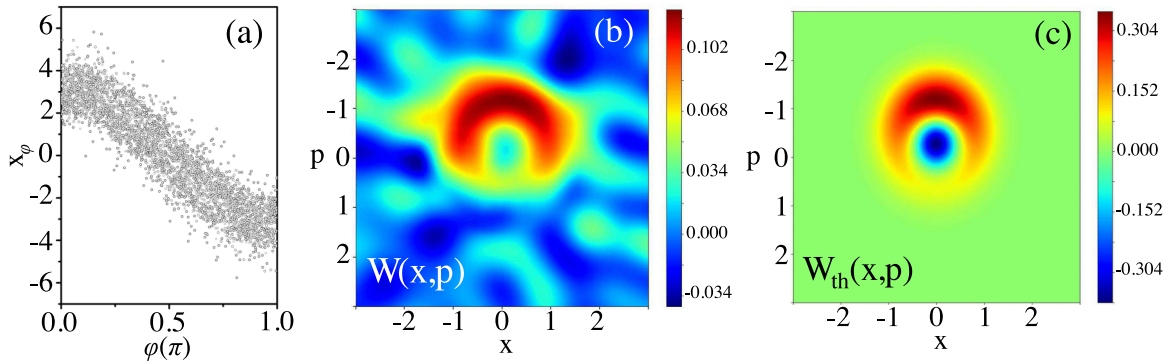


FIG. 8. High-photon-number optical “cat” state created by conditioning on HHG. (a) Measured \hat{x}_φ with xenon gas and QS switched on. (b) Projection on (x, p) plane of the reconstructed $W(x, p)$, which shows an optical “cat” state of $\langle n \rangle \approx 9.4 \pm 0.1$. (c) Theoretically calculated Wigner function $W_{\text{th}}(x, p)$ for $|\delta\alpha_L| \approx 0.8$, where $|\alpha_L| \approx 3.7$ and $|\xi| \approx 0.73$. x and p are the values of the quadrature field operators $\hat{x} = (\hat{a} + \hat{a}^\dagger)/\sqrt{2}$ and $\hat{p} = (\hat{a} - \hat{a}^\dagger)/i\sqrt{2}$. The Wigner functions in these plots have been centered around the value of α_L .

light state requires an extensive theoretical and experimental investigation, which is out of the scope of our work. The present results cannot be used for such analysis. However, in order to further stress the potential of our approach to produce high-photon-number shifted optical cat states in a lossy environment, we have used a simple, although exact, noise model that introduces photon losses due to the interaction with a Gaussian reservoir [68]. This is done by means of a beam splitter where in one of the inputs we introduce our cat state, while on the other an ancillary vacuum mode that is later traced out (for more details, see Appendix I). This model shows that, even in the case of high photon losses (in the range of 60%), although the negativity of the Wigner function of the optical cat state is reduced, the main features are maintained.

IV. DISCUSSION AND PERSPECTIVES

In the past two decades, pioneering optical methods in quantum state engineering have been implemented for the generation of optical catlike and cat states (cf. [13,15–18]). These methods rely on the use of few-photon-number and high-fidelity Fock states as primary sources, and they currently deliver optical cat states in the range of a few photon numbers, restricting their applicability in quantum technologies. This is because the quantum technology toolbox contains passive linear optical elements (such as phase shifters, beam splitters, and fiber optics), which unavoidably have optical losses. Thus, it is evident that any beam propagating through these elements will naturally suffer from photon losses. Hence, one of the main motivations for generating high-photon-number optical cat states (as we report here) is associated with their power to be used in more complex optical arrangements that can lead to the generation of large optical cat states and massively entangled state superpositions with controllable quantum features. Such states could highly benefit from investigations concerning the fundamental tests of quantum theory, quantum information processing, metrology/sensing, and communication. Toward these directions, we have recently reported how the method presented here can be used for the development of more complex optical arrangements that can lead to the generation of (i) controllable large coherent-state superpositions [61], and (ii) multimode

entangled states spanning from the near infrared to the extreme ultraviolet [58], which can be very useful for quantum technology.

Additionally, and in a more general context, the present findings can be used for linking the attosecond and quantum information science (ATTOQUIS) toward the establishment of a roadmap for novel platforms of attosecond science and quantum technologies. Contemporary quantum technologies face major difficulties in fault-tolerant quantum computing with error correction, and they focus instead on various shades of quantum simulation (Noisy Intermediate Scale Quantum devices [69], analog and digital Quantum Simulators [70], and quantum annealers [71]). There is a clear need and quest for such systems that, without necessarily simulating the dynamics of some quantum systems, can generate massive, controllable, robust, entangled, and superpositions states. This will enable the use of these states for quantum communications [72] (e.g., to achieve transfer of information in a safer and quicker way), quantum metrology [73], and sensing and diagnostics [74] (e.g., to precisely measure phase shifts of light fields, or to diagnose quantum materials). To date, there are no existing platforms that bring processes at such short timescales to quantum information science. ATTOQUIS can open the way for realizing universal and firmly established tools to offer novel solutions and developments, i.e., a set of methods to generate massive entangled states and massive quantum superpositions for applications in quantum information science, with the ultimate goal of bringing them to quantum technologies.

V. CONCLUSIONS

In this work, we investigated the quantum optics of strongly laser driven atoms. Using a fully quantized theoretical approach, we described the HHG and ATI processes, and we showed how the conditioning on HHG and ATI processes can naturally lead to the generation of amplitude-shifted coherent-state superpositions. Additionally, we have investigated the parameters that can be used to control the quantum features of these states. This was experimentally confirmed by measuring the quantum features of the coherent-state superposition obtained after conditioning on HHG for

different gas densities. We found that the coherent-state superposition changes from an optical “cat” to a “kitten” state as the number of atoms participating in the harmonic generation process is reduced. We also show that this procedure can be used for the generation of high-photon-number coherent-state superpositions. This has been experimentally confirmed by recording a nine-photon shifted optical “cat” state. Finally, considering that the strong field laser-atom interaction is at the core of strong laser-field physics, it can be considered that our work builds the basis for the development of a new class of controllable high-photon-number nonclassical light sources and for quantum optical studies of interactions induced in matter using laser intensities in the moderate and relativistic regions [43,75].

ACKNOWLEDGMENTS

We thank Jens Biegert, Ido Kaminer, and Pascal Salières for enlightening discussions. We also thank I. Lontos and E. Skantzakis from FORTH, and S. Karsch from Max Planck Institute for Quantum Optics for his assistance in maintaining the performance of the Ti:Sa laser system. ICFO group acknowledges support from ERC AdG NOQIA, from Agencia Estatal de Investigación (the R&D project CEX2019-000910-S, funded by MCIN/AEI/10.13039/501100011033, Plan National FIDEUA PID2019-106901GB-I00, FPI, QUANTERA MAQS PCI2019-111828-2, Proyectos de I+D+I “Retos Colaboración” RTC2019-007196-7) from Fundació Cellex, Fundació Mir-Puig, and from Generalitat de Catalunya through the CERCA program, AGAUR Grant No. 2017 SGR 134, QuantumCAT U16-011424, cofunded by ERDF Operational Program of Catalonia 2014-2020, EU Horizon 2020 FET-OPEN OPTOLogic (Grant No. 899794), and the National Science Centre, Poland (Symfonia Grant No. 2016/20/W/ST4/00314), European Union’s Horizon 2020 research and innovation programme under the Marie Skłodowska-Curie Grant Agreement No. 101029393 (STREDCH), “La Caixa” Junior Leaders fellowships (ID100010434), and EU Horizon 2020 under Marie Skłodowska-Curie Grant Agreement No. 847648 (LCF/BQ/PI19/11690013, LCF/BQ/PI20/11760031, LCF/BQ/PR20/11770012, LCF/BQ/PR21/11840013). FORTH group acknowledges LASERLABEUROPE (H2020-EU.1.4.1.2 Grant ID 654148), FORTH Synergy Grant AgiIDA (Grant No. 00133), and the EU’s H2020 framework programme for research and innovation under the NFFA-Europe-Pilot project (Grant No. 101007417). J.R.-D. acknowledges support from the Secretaria d’Universitats i Recerca del Departament d’Empresa i Coneixement de la Generalitat de Catalunya, as well as the European Social Fund (L’FSE inverteix en el teu futur)–FEDER. E.P. acknowledges support from Royal Society University Research Fellowship URFR1211390. P.S. acknowledges funding from the European Union’s Horizon 2020 research and innovation programme under the Marie Skłodowska-Curie grant agreement No. 847517. A.S.M. acknowledges funding support from the European Union’s Horizon 2020 research and innovation programme under the Marie Skłodowska-Curie grant agreement SSFI No. 887153. M.F.C. acknowledges support from the Guangdong Province Science

and Technology Major Project Future functional materials under extreme conditions—212019071820400001. P.T. group acknowledges LASERLABEUROPE V (H2020-EU.1.4.1.2 Grant No. 871124), FORTH Synergy Grant AgiIDA (Grant No. 00133), and the H2020 framework program for research and innovation under the NFFA-Europe-Pilot project (No. 101007417). ELI-ALPS is supported by the European Union and cofinanced by the European Regional Development Fund (GINOP Grant No. 2.3.6-15-2015-00001).

APPENDIX A: QUANTUM OPTICAL DESCRIPTION OF THE LASER-ATOM INTERACTION: TRANSFORMATIONS AND APPROXIMATIONS

Our starting point is the time-dependent Schrödinger equation (TDSE) describing the interaction of the quantized electromagnetic field with a single electron,

$$i\hbar \frac{\partial}{\partial t} |\tilde{\Psi}(t)\rangle = \hat{H}(t) |\tilde{\Psi}(t)\rangle, \quad (\text{A1})$$

where

$$\hat{H}(t) = \hat{H}_0 + \hat{H}_I + \hat{H}_f. \quad (\text{A2})$$

Here, $\hat{H}_0 = \hat{\mathbf{P}}^2/2m + V(\hat{\mathbf{R}})$ is the Hamiltonian describing the electron bound to a potential $V(\hat{\mathbf{R}})$, $\hat{H}_I = -e\hat{\mathbf{E}} \cdot \hat{\mathbf{R}}$ is the dipole coupling that introduces the interaction between the electron and the field in the dipole approximation, and \hat{H}_f is the electromagnetic free-field Hamiltonian. In the following, we will represent the electronic quadrature operators with capital letters (\hat{X} , \hat{P}), while the photonic ones will be denoted with lower-case letters (\hat{x} , \hat{p}).

As we aim to describe laser/harmonic pulses of finite duration, we should consider in the free-field term \hat{H}_f the full continuum spectrum of the electromagnetic field. Nevertheless, for the sake of simplicity, we write it as the sum of effective discrete modes containing the one obtained from the laser with frequency ω_L and its harmonics of frequencies $\omega_q = q\omega_L$, with $q = 1, 2, 3, \dots$ up to the cutoff region of the spectrum. Concretely, we have

$$\hat{H}_f = \hbar\omega_L \hat{a}^\dagger \hat{a} + \sum_{q=2}^{\text{cutoff}} \hbar q\omega_L \hat{b}_q^\dagger \hat{b}_q, \quad (\text{A3})$$

where \hat{a}^\dagger (\hat{a}) and \hat{b}_q^\dagger (\hat{b}_q) are the creation (annihilation) operators acting over the laser and the q th harmonic mode, respectively. Following the same idea, we model the laser electric field operator as

$$\hat{\mathbf{E}}(t) = -i\hbar\mathbf{g}(\omega_L)f(t) \left[(\hat{a}^\dagger - \hat{a}) + \sum_{q=2}^{\text{cutoff}} \sqrt{q}(\hat{b}_q^\dagger - \hat{b}_q) \right]. \quad (\text{A4})$$

Here, we denote by $\mathbf{g}(\omega_L) \propto \sqrt{\omega_L/V_{\text{eff}}}$ the coefficient that enters into the expansion of the laser electric field modes and that depends on V_{eff} , which is the effective quantization volume [5,52]. Thus, $\mathbf{e}\mathbf{g}(\omega_L)$ encodes information about the polarization modes and has dimensions ($\text{m}^{-1} \text{s}^{-1}$). Finally, $0 \leq f(t) \leq 1$ is a dimensionless function describing the pulse envelope.

At time $t = t_0$, we can describe the state of the system by $|\Psi(t_0)\rangle = |g, \alpha_L, \Omega_H\rangle$, that is, with the electron lying on the atomic ground state, the laser mode in a coherent-state, and the harmonic modes in the vacuum state. Within this context, the first transformation we apply consists of moving to the interaction picture with respect to the electromagnetic field \hat{H}_f , i.e.,

$$|\tilde{\Psi}(t)\rangle = \exp[-i\hat{H}_f t]|\Psi'(t)\rangle, \quad (\text{A5})$$

so that Eq. (A1) reads

$$i\hbar \frac{\partial}{\partial t} |\Psi'(t)\rangle = [\hat{H}_0 - \mathbf{e}\hat{\mathbf{E}}(t) \cdot \hat{\mathbf{R}}]|\Psi'(t)\rangle, \quad (\text{A6})$$

where the laser electric field operator defined in Eq. (A4) has an extra time dependence

$$\begin{aligned} \hat{\mathbf{E}}(t) = & -i\hbar \mathbf{g}(\omega_L) f(t) [(\hat{a}^\dagger e^{i\omega_L t} - \hat{a} e^{-i\omega_L t}) \\ & + \sum_{q=2}^{\text{cutoff}} \sqrt{q} (\hat{b}_q^\dagger e^{iq\omega_L t} - \hat{b}_q e^{-iq\omega_L t})]. \end{aligned} \quad (\text{A7})$$

The second transformation we apply consists of a displacement in the subspace of the driving laser field of a quantity α_L , i.e.,

$$|\Psi'(t)\rangle = \hat{D}(\alpha_L)|\Psi(t)\rangle, \quad (\text{A8})$$

where $\hat{D}(\alpha_L)$ is the optical displacement operator [5], acting over the laser mode. Recalling the following properties of this operator [4]:

$$\hat{D}(\alpha)^\dagger \hat{D}(\alpha) = \mathbb{1}, \quad (\text{A9})$$

$$\hat{D}(\alpha) \hat{a} \hat{D}^\dagger(\alpha) = \hat{a} - \alpha, \quad (\text{A10})$$

its introduction in our equations has two mutually related consequences: it sets the initial state of the laser mode to a vacuum state Ω_L , and it transforms our TDSE into

$$\begin{aligned} i\hbar \frac{\partial}{\partial t} |\Psi(t)\rangle = & [\hat{H}_0 - \mathbf{e}\mathbf{E}_L(t) \cdot \hat{\mathbf{R}} - \mathbf{e}\hat{\mathbf{E}}_Q(t) \cdot \hat{\mathbf{R}}]|\Psi(t)\rangle \\ = & [\hat{H}_{\text{sc}} - \mathbf{e}\hat{\mathbf{E}}_Q(t) \cdot \hat{\mathbf{R}}]|\Psi(t)\rangle. \end{aligned} \quad (\text{A11})$$

Here, $\mathbf{E}_L(t)$ accounts for the classical electric field part of the laser pulse

$$\mathbf{E}_L(t) = -i\hbar \mathbf{g}(\omega_L) f(t) [\alpha_L^* e^{i\omega_L t} - \alpha_L e^{-i\omega_L t}], \quad (\text{A12})$$

so \hat{H}_{sc} represents the semiclassical part of our Hamiltonian [22]. On the other hand, $\hat{\mathbf{E}}_Q(t)$ is the quantum correction term defined as in Eq. (A7).

Lastly, we move to the interaction picture with respect to the semiclassical Hamiltonian \hat{H}_{sc} ,

$$|\Psi(t)\rangle = \mathcal{T} \exp \left[-i \int_{t_0}^t dt' \hat{H}_{\text{sc}}(t') / \hbar \right] |\psi(t)\rangle, \quad (\text{A13})$$

where \mathcal{T} is the time-ordering operator. This last transformation leads us to the final form of our TDSE, which we will use throughout this manuscript, i.e.,

$$i\hbar \frac{\partial}{\partial t} |\psi(t)\rangle = -\mathbf{e}\hat{\mathbf{E}}_Q(t) \cdot \hat{\mathbf{R}}_H(t) |\psi(t)\rangle, \quad (\text{A14})$$

where $\mathbf{e}\hat{\mathbf{R}}_H(t)$ denotes the time-dependent dipole operator in the considered semiclassical interaction picture, acting exclusively on the electronic degrees of freedom. This evolution drives the dynamics of the field and the electron, which may end up in the ground or continuum states. On the other hand, we consider that the electron will rarely end up in a bound-excited state.

APPENDIX B: QUANTUM OPTICAL DESCRIPTION OF HIGH-HARMONIC GENERATION

In the HHG process, the electron gets first transferred to the continuum via tunneling ionization due to the strong laser field we are applying, and later on it recombines with the parent ion that was left behind, ending up again in the ground state of the system. Therefore, in order to get information about the HHG photonic quantum state, we condition Eq. (A14) onto the atomic ground state $|g\rangle$, i.e.,

$$i\hbar \frac{\partial}{\partial t} \langle g | \psi(t) \rangle = -\hat{\mathbf{E}}_Q(t) \cdot \langle g | \mathbf{e}\hat{\mathbf{R}}_H(t) | \psi(t) \rangle. \quad (\text{B1})$$

Defining the identity operator as

$$\mathbb{1} = |g\rangle \langle g| + \sum_{\phi_b} |\phi_b\rangle \langle \phi_b| + \int d\phi_c |\phi_c\rangle \langle \phi_c|, \quad (\text{B2})$$

where we denote with the discrete sum the set of atomic bound excited states, and with the integral the set of continuum states, we introduce it in Eq. (B1) to get

$$\begin{aligned} i\hbar \frac{\partial}{\partial t} \langle g | \psi(t) \rangle = & -\hat{\mathbf{E}}_Q(t) \cdot \left[\mathbf{d}_H(t) \langle g | \psi(t) \rangle \right. \\ & + \sum_{\phi_b} \mathbf{d}_H(\phi_b, t) \langle \phi_b | \psi(t) \rangle \\ & \left. + \int d\phi_c \mathbf{d}_H(\phi_c, t) \langle \phi_c | \psi(t) \rangle \right]. \end{aligned} \quad (\text{B3})$$

In this last expression, we denote with $\mathbf{d}_H(t) = \langle g | \mathbf{e}\hat{\mathbf{R}}_H(t) | g \rangle$ the quantum averaged time-dependent dipole moment and with $\mathbf{d}_H(\phi_k, t) = \langle g | \mathbf{e}\hat{\mathbf{R}}_H(t) | \phi_k \rangle$ the matrix element between the ground state and state $|\phi_k\rangle$, where k can take values b or c depending on whether the state belongs to the bound excited states or to the continuum region of the spectrum, respectively. Each of these terms is multiplied by the probability amplitude of finding the electron either in the ground state, in another excited bound state, or in an excited continuum state. In the first attempt to solve the problem, we will assume that these two last terms are very small in comparison to the first one, which is a fair assumption as the electron hardly remains in an excited bound/continuum state [22,23] at the end of the pulse. Therefore, our TDSE adopts the following form:

$$i\hbar \frac{\partial}{\partial t} |\Phi(t)\rangle = -\hat{\mathbf{E}}_Q(t) \cdot \mathbf{d}_H(t) |\Phi(t)\rangle, \quad (\text{B4})$$

where $|\Phi(t)\rangle = \langle g | \psi(t) \rangle$. Here, $\mathbf{d}_H(t)$ can be easily calculated by numerically solving the TDSE, or by means of the strong-field approximation (SFA) theory [22,23,53]. Whatever the method used, this equation can be easily solved as it is written

as a linear combination of photon creation and annihilation operators for the different modes considered in the problem. This has a natural implication, which is that the final solution is given by a product state of all the modes participating in the process,

$$|\Phi(t)\rangle = |\Phi_{q=1}(t)\rangle \otimes |\Phi_{q=2}(t)\rangle \otimes \cdots \otimes |\Phi_{q=\text{cutoff}}(t)\rangle, \quad (\text{B5})$$

so we can solve the equation for a given q and then generalize the result to the rest. Thus, the single-mode version of Eq. (B4) which we will now deal with is

$$i\hbar \frac{\partial}{\partial t} |\Phi_q(t)\rangle = -\hat{\mathbf{E}}_q(t) \cdot \mathbf{d}_H(t) |\Phi_q(t)\rangle = \hat{H}_q(t) |\Phi_q(t)\rangle, \quad (\text{B6})$$

where

$$\hat{\mathbf{E}}_q(t) = -i\hbar \mathbf{g}(\omega_L) f(t) \sqrt{q} [\hat{b}_q^\dagger e^{iq\omega_L t} - \hat{b}_q e^{-iq\omega_L t}]. \quad (\text{B7})$$

In general, we can write the solution to this equation as [76]

$$|\Phi_q(t)\rangle = \hat{U}_q(t, t_0) |\Phi_q(t_0)\rangle, \quad (\text{B8})$$

where $\hat{U}(t, t_0)$ is our time-evolution operator. Furthermore, we can split our time interval in N steps of size Δt , which is typically defined to be inversely proportional to N , such that we can write this operator as

$$\hat{U}_q(t, t_0) = \lim_{N \rightarrow \infty} \prod_{i=0}^{N-1} \hat{U}_q(t_{i+1}, t_i), \quad (\text{B9})$$

where we identify $t_N = t$. Therefore, we can write each of the unitary operators appearing in the previous product as

$$\hat{U}_q(t_{i+1}, t_i) = \exp[-i\hat{H}_q(t_{i+1})\Delta t/\hbar]. \quad (\text{B10})$$

Let us take a closer look at the commutation relation between $\hat{H}_q(t)$ defined at two different times t and t' ,

$$\begin{aligned} i[\hat{H}_q(t), \hat{H}_q(t')] &= -2q\hbar^2 f(t)f(t') \\ &\times (\mathbf{g}(\omega_L) \cdot \mathbf{d}_H(t))(\mathbf{g}(\omega_L) \cdot \mathbf{d}_H(t')) \\ &\times \sin(q\omega_L(t - t')). \end{aligned} \quad (\text{B11})$$

As we can see, this term is a function proportional to the identity operator, something that favors the implementation of the Baker-Campbell-Hausdorff (BCH) formula [6], i.e.,

$$e^{\hat{X}} e^{\hat{Y}} = e^{\hat{Z}}, \quad (\text{B12})$$

where

$$\hat{Z} = \hat{X} + \hat{Y} + \frac{1}{2}[\hat{X}, \hat{Y}] + \frac{1}{12}[\hat{X}, [\hat{X}, \hat{Y}]] + \cdots, \quad (\text{B13})$$

to join all the exponential operators in Eq. (B9), as we only have to keep the first three terms on the right-hand side of Eq. (B13) since all the other terms commute. Notice that each time we join two consecutive operators, we get an extra exponential term from the commutation relation in Eq. (B11). The exponent of such a term adopts the following form:

$$i\varphi_q(t) = -\frac{i}{2} \sum_{j=1}^{N-1} \sum_{i=0}^j [\hat{H}_q(t_j), \hat{H}_q(t_i)] \Delta t^2 / \hbar^2 \quad (\text{B14})$$

and the final time-evolution operator reads

$$\hat{U}_q(t, t_0) = \lim_{N \rightarrow \infty} \exp[-i \left(\sum_{i=0}^{N-1} \hat{H}_q(t_i) \right) \Delta t / \hbar] e^{i\varphi_q(t)}, \quad (\text{B15})$$

where in the exponential operator term we naturally recover the definition of an integral. Thus, according to the definition of $\hat{H}_q(t)$ given in Eq. (B6), the previous unitary operator can be written, for the case of the fundamental mode ($q = 1$), as

$$\hat{U}_L(t, t_0) = \exp[\delta\alpha_L \hat{a}^\dagger - \delta\alpha_L^* \hat{a}] e^{i\varphi_L(t)}, \quad (\text{B16})$$

which is a displacement in the photonic phase space of a quantity $\delta\alpha_L$ defined by

$$\delta\alpha_L(t) = \mathbf{g}(\omega_L) \cdot \int_{t_0}^t d\tau f(\tau) \mathbf{d}_H(\tau) e^{i\omega_L \tau}. \quad (\text{B17})$$

Therefore, incorporating the action of Eq. (B15) over the harmonic modes, we finally get the final quantum optical HHG state,

$$\begin{aligned} |\Phi(t)\rangle &= e^{i\varphi_L(t)} |(\alpha_L + \delta\alpha_L) e^{-i\omega_L t}\rangle \otimes e^{i\varphi_2(t)} |\beta_2 e^{-i2\omega_L t}\rangle \\ &\otimes \cdots \otimes e^{i\varphi_q(t)} |\beta_q e^{-iq\omega_L t}\rangle \otimes \cdots, \end{aligned} \quad (\text{B18})$$

where we have returned to the original photonic frame of reference, that is, we have undone the initial transformations depicted in Eqs. (A5) and (A8). Note that here the $i\varphi_q(t)$ are defined as in Eq. (B14) once the limit $N \rightarrow \infty$ has been considered. Similarly to the $\delta\alpha_L$, the β_q terms are defined as

$$\beta_q(t) = \sqrt{q} \mathbf{g}(\omega_L) \cdot \int_{t_0}^t d\tau f(\tau) \mathbf{d}_H(\tau) e^{iq\omega_L \tau}. \quad (\text{B19})$$

The results obtained until now are valid for the single-atom case. For the N -atomic case, assuming that each atom contributes to the HHG process coherently in a phase-matched way, the definitions of $\delta\alpha_L$ and β_q are reformulated as

$$\delta\alpha_L(t) = N \mathbf{g}(\omega_L) \cdot \int_{t_0}^t d\tau f(\tau) \mathbf{d}_H(\tau) e^{i\omega_L \tau}, \quad (\text{B20})$$

$$\beta_q(t) = N \sqrt{q} \mathbf{g}(\omega_L) \cdot \int_{t_0}^t d\tau f(\tau) \mathbf{d}_H(\tau) e^{iq\omega_L \tau}. \quad (\text{B21})$$

Note that in this case, the N -atomic wave function will be affected by an overall phase coming from the BCH relation that does not affect the phase-matching conditions, which are solely determined by the phase of the generated coherent states. To give a physical meaning to $\delta\alpha_L$ and β_q within the electron recollision picture, we will use the strong-field approximation theory to provide a solution to the integrals in Eqs. (B20) and (B21). According to the SFA, it can be shown [22] that the mean value of the dipole operator $\mathbf{d}_H(t)$ reads

$$\begin{aligned} \mathbf{d}_H(t) &= i \int_{t_0}^t dt' \int d\mathbf{v} \mathbf{d}^* \left(\mathbf{p} - \frac{e}{c} \mathbf{A}_L(t') \right) e^{-iS(\mathbf{p}, t, t')} \\ &\times E_L(t') \mathbf{d} \left(\mathbf{p} - \frac{e}{c} \mathbf{A}_L(t') \right) + \text{c.c.}, \end{aligned} \quad (\text{B22})$$

where $\mathbf{A}_L(t)$ is the vector potential of the laser field defined as $E_L(t) = -(1/c) \partial \mathbf{A}_L(t) / \partial t$, $\mathbf{p} = \mathbf{v} + (e/c) \mathbf{A}_L(t)$ is the canonical momentum whereas \mathbf{v} is the electron's kinetic momentum,

$\mathbf{d}(\mathbf{p} - (e/c)\mathbf{A}_L(t'))$ is the matrix element of the dipole operator between the atomic ground state and the continuum state $|\mathbf{p} - (e/c)\mathbf{A}_L(t')\rangle$, and $S(\mathbf{p}, t, t')$ is the semiclassical action given by

$$S(\mathbf{p}, t, t') = \frac{1}{2} \int_{t'}^t d\tau \left[\mathbf{p} - \frac{e}{c}\mathbf{A}_L(\tau) \right]^2 + I_p(t - t'), \quad (\text{B23})$$

where I_p is the ionization potential.

For the sake of simplicity, we will assume that the used laser field consists of a monochromatic field of frequency ω_L , so that we can set $f(t) = 1$ in Eqs. (B20) and (B21), which now read

$$\delta\alpha_L(t) = N\mathbf{g}(\omega_L) \cdot \int_{t_0}^t d\tau \mathbf{d}_H(\tau)e^{i\omega_L\tau}, \quad (\text{B24})$$

$$\beta_q(t) = N\sqrt{q}\mathbf{g}(\omega_L) \cdot \int_{t_0}^t d\tau \mathbf{d}_H(\tau)e^{iq\omega_L\tau}. \quad (\text{B25})$$

The semiclassical action shown in Eq. (B23) is a highly oscillating function that leads to a highly oscillating exponent in Eq. (B22), and allows for a solution to the triple integration appearing in Eqs. (B24) and (B25) by means of the saddle-point approximation. Therefore, the integrals in Eqs. (B24) and (B25) are completely characterized by the saddle points determined by the set of variables (\mathbf{p}_s, t_r, t_i) fixed by the following three equations, which have been extensively studied in the past within the context of the semiclassical three-step model [22,23]:

$$\frac{[\mathbf{p}_s - \frac{e}{c}\mathbf{A}_L(t_i)]^2}{2} + I_p = 0, \quad (\text{B26})$$

$$\int_{t_i}^{t_r} d\tau \left[\mathbf{p}_s - \frac{e}{c}\mathbf{A}_L(\tau) \right] = 0, \quad (\text{B27})$$

$$\frac{[\mathbf{p}_s - \frac{e}{c}\mathbf{A}_L(t_r)]^2}{2} + I_p = q\omega_L. \quad (\text{B28})$$

In brief terms, the above equations define the three steps of the recollision process: (B26) defines the ionization time t_i , (B27) the electron's return to the parent ion, and (B28) the recombination time t_r associated with the generation of high harmonics with frequencies $q\omega_L > I_p$. On the one hand, these equations imply that the shift $\delta\alpha_L$ of the coherent state is directly related to the electron ionization and acceleration processes. On the other hand, they also show that the well-known features of the HHG process are transferred to the coherent states of the harmonic field, that is, the β_q 's contain information about the spectral phase and amplitude distribution of the emitted harmonics. In fact, this can be shown by calculating the spectrum of the generated harmonics, which can be obtained from their energy $\langle \hat{H}_f \rangle_{\text{em}} = \sum_q \hbar\omega_q n_q$. In this expression, n_q is the number of photons at frequency $\omega_q = q\omega_L$, which, according to Eq. (B21), is given by

$$n_q = N^2 |\mathbf{g}(\omega_q) \cdot \mathbf{d}_H(q\omega_L)|^2. \quad (\text{B29})$$

To obtain Eq. (B29), we have sent the integration limits to $\pm\infty$, implying that the electric field is introduced at $t_0 = -\infty$ and lasts until $t = +\infty$, so that the integral appearing

in Eq. (B25) represents the Fourier transform of the mean-valued dipole $\mathbf{d}_H(q\omega_L)$. Considering all possible frequencies, its summation can be rewritten as an integral, and the energy of the emitted harmonics reads

$$E_{\text{em}} = \frac{V_{\text{eff}}}{(2\pi c)^3} \int d\Omega d\omega N^2 \omega^3 |\mathbf{g}(\omega) \cdot \mathbf{d}_H(\omega)|^2, \quad (\text{B30})$$

where $d\Omega$ represents the infinitesimal solid angle element. Substituting the definition of $\mathbf{g}(\omega_L)$ into Eq. (B30), we find for its integrand

$$\mathcal{E}_{\text{HHG}}(\omega_q) \propto N^2 \omega_q^4 |\mathbf{d}_H(\omega_q)|^2, \quad (\text{B31})$$

which corresponds to the expression of the HHG spectrum obtained by the semiclassical theory [22,23].

APPENDIX C: ANALYSIS OF THE COHERENT SHIFT IN THE FUNDAMENTAL MODE

As mentioned in the text and explicitly developed in Appendix B, the shift in the fundamental mode $\delta\alpha_L$ is related to the absorbed part of the driving field that is necessary for generating the harmonic photons; its properties can be related to the exchange of photons during the interaction. In particular, we are interested in the probability of absorbing n photons during the ionization and acceleration processes. For that reason, we consider a coherent state $|\delta\alpha_L(t, t_0)\rangle$ and compute the probability distribution of having n photons on it

$$\begin{aligned} P_n(t, t_0) &= |\langle n | \delta\alpha_L(t, t_0) \rangle|^2 \\ &= \frac{|\delta\alpha_L(t, t_0)|^{2n}}{n!} e^{-|\delta\alpha_L(t, t_0)|^2}. \end{aligned} \quad (\text{C1})$$

We note that this quantity is related to the probability of absorbing n photons during the ionization and acceleration processes. We further introduce the average probability of having n photons in the above coherent state within a cycle of the field that starts at t_0 and finishes at time T as

$$\tilde{P}_n = \frac{1}{T - t_0} \int_{t_0}^T dt P_n(t, t_0). \quad (\text{C2})$$

The numerical results obtained from this calculation are shown in Fig. 9 for three different intensities of the driving field. As we can see, for each of the curves we get a local maximum in the probability that shifts to bigger values of the number of photons n as the intensity of the field increases. This is consistent with the harmonic plateau structure obtained for the HHG spectrum. As the intensity increases, the harmonic cutoff is extended to higher photon number values and, as a consequence, photons of higher frequency are achievable through the HHG process. Thus, given that for generating a photon of frequency $n\omega_L$ a number n of IR photons need to be absorbed, then in order to get a plateau structure for the harmonic spectrum, the probability of absorbing IR photons should increase as we move toward the harmonic cutoff, reaching a maximum at this point and decreasing afterwards. To check this, we look at the value of n for which we find a local maximum in the probability (the maximum obtained for $n > 2$) for each of the considered intensities. In particular, in Fig. 9 these maxima are placed at $n_{\text{cutoff}} \approx 7, 12,$ and 15 from the lowest to the highest intensity, respectively, which

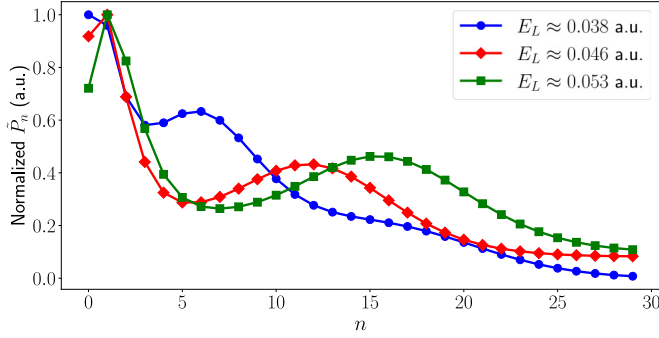


FIG. 9. Probability of having n photons in the coherent state $|\delta\alpha_L\rangle$ averaged in time. Normalized average probability of a single atom to absorb n photons for three different electric field amplitudes, $E_L \approx 0.053$ a.u. (green squared-dotted curve), $E_L \approx 0.046$ a.u. (red rhomboid-dotted curve), and $E_L \approx 0.038$ a.u. (blue round-dotted curve) of the driving field (in atomic units). The results have been obtained by integrating over one cycle of a Gaussian-shaped pulse with central wavelength $\lambda_L = 800$ nm.

are in agreement with the cutoffs given by the maximum kinetic energy that an electron can get in the HHG process with the corresponding intensities (the theoretical values for the cutoff are $n_{\text{th}} = 7.71, 11.3,$ and 15.0 , respectively). Note that in comparison to Eq. (B31), here we do not obtain a multipeak structure involving only the odd harmonics. This is because $\delta\alpha$ describes the amount of IR photons absorbed during the ionization and acceleration processes affecting the fundamental laser mode, which later on will be distributed along the generated harmonics.

APPENDIX D: CONDITIONING ONTO HHG: GENERATION OF SCHRÖDINGER OPTICAL “KITTEN” AND “CAT” STATES

As mentioned in the main text, the time-evolved state obtained after conditioning the electron state to be end up in the ground state of the system is given by

$$|\Phi(t)\rangle = e^{i\varphi_L(t)}|\alpha_L + \delta\alpha_L\rangle e^{-i\omega_L t} \otimes e^{i\varphi_2(t)}|\beta_2\rangle e^{-i2\omega_L t} \otimes \dots \otimes e^{i\varphi_q(t)}|\beta_q\rangle e^{-iq\omega_L t} \otimes \dots, \quad (\text{D1})$$

The key action for creating the nonclassical states of light is the postselection of the coherent shifted IR state over the part that includes at least one harmonic photon. It was shown in [58] that conditioning the harmonic modes to be found in the state $\bigotimes_{q=2}^{\text{cutoff}} |\beta_q\rangle$ and considering very high values of the harmonic cutoff, the final quantum optical state of the infrared mode is given by (up to normalization) by

$$|\Phi_{\text{post}}\rangle \approx |\alpha_L + \delta\alpha_L\rangle - \langle\alpha_L|\alpha_L + \delta\alpha_L\rangle|\alpha_L\rangle. \quad (\text{D2})$$

In the following, we will explicitly develop the different situations studied in the main text that lead us to the generation of Schrödinger optical “kitten” and cat states.

1. Obtaining a “kitten” state

The kitten state is obtained in the limit when $\langle\alpha_L|\alpha_L + \delta\alpha_L\rangle \rightarrow 1$, which corresponds to the limit where $|\delta\alpha_L| \rightarrow 0$. This is valid whenever $\delta\alpha$ adds a depletion to

the initial coherent state, a condition that is verified when the phases of $\delta\alpha$ and α , which we denote here as θ_δ and θ_α , respectively, satisfy

$$\frac{\pi}{2} + \arcsin\left(\frac{|\delta\alpha_L|}{2|\alpha_L|}\right) + \theta_\alpha < \theta_\delta < \frac{3\pi}{2} - \arcsin\left(\frac{|\delta\alpha_L|}{2|\alpha_L|}\right) + \theta_\alpha. \quad (\text{D3})$$

To work in regimes of vanishing $|\delta\alpha_L|$, we will consider an expansion of the postprocessed state presented in Eq. (D2) in terms of powers of $|\delta\alpha_L|$. With that purpose, we first write our shifted coherent state $|\alpha_L + \delta\alpha_L\rangle$ as

$$|\alpha_L + \delta\alpha_L\rangle = \hat{D}(\alpha_L)e^{\frac{1}{2}(\alpha_L^*\delta\alpha_L - \alpha_L\delta\alpha_L^*)}\hat{D}(\delta\alpha_L)|0\rangle, \quad (\text{D4})$$

where we have considered the following property of the displacement operator:

$$\hat{D}(\alpha_L + \delta\alpha_L) = e^{\frac{1}{2}(\alpha_L^*\delta\alpha_L - \alpha_L\delta\alpha_L^*)}\hat{D}(\alpha_L)\hat{D}(\delta\alpha_L). \quad (\text{D5})$$

Introducing here the definition of the displacement operator $D(\alpha)$ and in particular its polynomial expansion,

$$\begin{aligned} \hat{D}(\delta\alpha_L) &= \exp[\delta\alpha_L\hat{a}^\dagger - \delta\alpha_L^*\hat{a}] \\ &= \sum_{n=0}^{\infty} \frac{(\delta\alpha_L\hat{a}^\dagger - \delta\alpha_L^*\hat{a})^n}{n!} \\ &= \sum_{n=0}^{\infty} |\delta\alpha_L|^n \frac{(e^{i\theta_\delta}\hat{a}^\dagger - e^{-i\theta_\delta}\hat{a})^n}{n!}, \end{aligned} \quad (\text{D6})$$

which, introduced in Eq. (D4), leads to the desired polynomial expansion in $|\delta\alpha|$,

$$\begin{aligned} |\alpha_L + \delta\alpha_L\rangle &= \hat{D}(\alpha_L)e^{\frac{1}{2}(\alpha_L^*\delta\alpha_L - \alpha_L\delta\alpha_L^*)} \\ &\times \sum_{n=0}^{\infty} |\delta\alpha_L|^n \frac{(e^{i\theta_\delta}\hat{a}^\dagger - e^{-i\theta_\delta}\hat{a})^n}{n!}|0\rangle, \end{aligned} \quad (\text{D7})$$

and whose scalar product with $|\alpha_L\rangle$ is given by

$$\begin{aligned} \langle\alpha|\alpha_L + \delta\alpha_L\rangle &= e^{\frac{1}{2}(\alpha_L^*\delta\alpha_L - \alpha_L\delta\alpha_L^*)}\langle 0|\delta\alpha_L\rangle \\ &= e^{\frac{1}{2}(\alpha_L^*\delta\alpha_L - \alpha_L\delta\alpha_L^*)}e^{-|\delta\alpha_L|^2/2} \\ &= e^{\frac{1}{2}(\alpha_L^*\delta\alpha_L - \alpha_L\delta\alpha_L^*)} \sum_{n=0}^{\infty} \frac{1}{2^n} \frac{|\delta\alpha_L|^{2n}}{n!}. \end{aligned} \quad (\text{D8})$$

Combining Eqs. (D7) and (D8) with Eq. (D2), we then get

$$\begin{aligned} |\Phi_{\text{post}}\rangle &= e^{\frac{1}{2}(\alpha_L^*\delta\alpha_L - \alpha_L\delta\alpha_L^*)}\hat{D}(\alpha_L) \\ &\times \sum_{n=1}^{\infty} \left(|\delta\alpha_L|^n \frac{(e^{i\theta_\delta}\hat{a}^\dagger - e^{-i\theta_\delta}\hat{a})^n}{n!} - \frac{1}{2^n} \frac{|\delta\alpha_L|^{2n}}{n!} \right) |0\rangle, \end{aligned} \quad (\text{D9})$$

where we start the sum at $n = 1$ because the $n = 0$ term cancels due to the equal contribution of the two terms in the difference. Thus, the previous difference leads to

$$\begin{aligned} |\Phi_{\text{post}}\rangle &= e^{\frac{1}{2}(\alpha_L^*\delta\alpha_L - \alpha_L\delta\alpha_L^*)}\hat{D}(\alpha_L) \\ &\times (\delta\alpha_L\hat{a}^\dagger|0\rangle + O(|\delta\alpha_L|^2)), \end{aligned} \quad (\text{D10})$$

which up to first order in $|\delta\alpha|$ corresponds with the definition of a displaced Fock state. Furthermore, we note that the photon number probability distribution of this state is given by

$$P(n) = \left| \frac{n}{\alpha_L} - \alpha_L^* \right|^2 \frac{|\alpha_L|^{2n}}{n!} e^{-|\alpha_L|^2}, \quad (\text{D11})$$

and its Wigner function [6] is characterized by

$$\begin{aligned} W(\beta) &= \frac{2}{\pi} \text{tr}(\hat{D}(\beta)\hat{\Gamma}\hat{D}(-\beta)|\Phi_{\text{post}}\rangle\langle\Phi_{\text{post}}|) \\ &= \frac{2}{\pi} (4|\beta - \alpha_L|^2 - 1)e^{|\beta - \alpha_L|^2/2}. \end{aligned} \quad (\text{D12})$$

For obtaining this expression, we have used the Wigner function definition of Ref. [77], where $\hat{\Gamma}$ denotes the parity operator, whose action over the displacement operator is given by $D(-\alpha) = \Pi D(\alpha)\Pi$.

2. Obtaining a genuine “cat” state

On the other hand, in the regime where $0 < \langle\alpha_L + \delta\alpha_L|\alpha_L\rangle < 1$, we obtain a genuine “cat” state [shown in Eq. (D1)] with photon number probability distribution

$$\begin{aligned} P(n) &= \frac{1}{N_{\text{cat}}} |(\alpha_L + \delta\alpha_L)^n e^{-|\alpha_L + \delta\alpha_L|^2/2} \\ &\quad - \langle\alpha_L|\alpha_L + \delta\alpha_L\rangle \alpha^n e^{-|\alpha_L|^2/2}|^2, \end{aligned} \quad (\text{D13})$$

and Wigner function

$$\begin{aligned} W(\beta) &= \frac{2}{\pi N_{\text{cat}}} \left[e^{-2|\beta - \alpha_L - \delta\alpha_L|^2} + e^{-|\delta\alpha_L|^2} e^{-2|\beta - \alpha_L|^2} \right. \\ &\quad \left. - (e^{2(\beta - \alpha_L)\delta\alpha_L^*} + e^{2(\beta - \alpha_L)^*\delta\alpha_L}) \right. \\ &\quad \left. \times e^{-|\delta\alpha_L|^2} e^{-2|\beta - \alpha_L|^2} \right], \end{aligned} \quad (\text{D14})$$

where $N_{\text{cat}} = 1 - e^{-|\delta\alpha_L|^2}$ is the normalization factor for Eq. (D2).

We finally note that in the regime where $|\delta\alpha_L|$ becomes large enough so that $\langle\alpha_L|\alpha_L + \delta\alpha_L\rangle \rightarrow 0$, we get a coherent shifted state with photon number probability distribution given by a Poissonian

$$P(n) = e^{-|\alpha_L + \delta\alpha_L|^2} \frac{|\alpha_L + \delta\alpha_L|^{2n}}{n!}, \quad (\text{D15})$$

and Wigner function

$$W(\beta) = \frac{2}{\pi N_{\text{cat}}} e^{-2|\beta - \alpha_L - \delta\alpha_L|^2}. \quad (\text{D16})$$

APPENDIX E: QUANTUM OPTICAL DESCRIPTION OF ABOVE-THRESHOLD IONIZATION

We showed in the main text that, under the strong-field approximations and within the single active electron scenario, the quantum optical state conditioned to ATI is given by

$$|\tilde{\Phi}(\mathbf{v}, t)\rangle \approx \frac{i}{\hbar} \sum_{j=0}^{N-1} \int_{t_j}^{t_{j+1}} dt' \hat{\mathbf{E}}_L(t') \cdot \mathbf{d}_H^*(\mathbf{v}, t') |(j+1)\Delta\rangle, \quad (\text{E1})$$

where $|\Phi(t)\rangle$ is given by Eq. (D1) before going back to the laboratory frame (which we get by setting $\alpha_L = 0$ in the mentioned state).

In the main text, we consider two possible strategies for deriving the reduced density matrix of the electromagnetic field after conditioning to ATI:

(i) We can condition on ATI electrons with a specific outgoing direction and kinetic momentum, \mathbf{v} . In this approach the reduced density matrix of the system is given by

$$|\Phi(\mathbf{v}, t)\rangle\langle\Phi(\mathbf{v}, t)|, \quad (\text{E2})$$

but the experimental detection is clearly tougher: even at fixed kinetic momentum with some error tolerance, there are not so many electrons to detect. We term this case *single-ionization ATI states*.

(ii) Alternatively, we can condition on all ATI electrons, i.e., consider the reduced density matrix integrated over all outgoing momenta,

$$\int d^3\mathbf{v} |\Phi(\mathbf{v}, t)\rangle\langle\Phi(\mathbf{v}, t)|. \quad (\text{E3})$$

Calculations and theoretical description are then more complex, but detection is easier.

In the following, we explicitly elaborate on the calculations that lead to the states presented in the main text when considering these two different scenarios.

1. Analysis for single-ionization ATI states

The state shown in Eq. (E1) is a superposition of the different coherent shifts generated during the ionization and acceleration processes, each of them multiplied by the matrix element $\mathbf{d}_H^*(\mathbf{v}, t')$, which determines its correlation with the electron's state, associating each shift with the probability amplitude of having a transition from the ground state to the continuum state $|\mathbf{v}\rangle$. However, this state only considers transitions to a particular continuum state.

In this subsection, we are going to consider single-ionization phenomena, i.e., laser ionization phenomena at a given kinetic momentum energy, corresponding to outgoing velocity \mathbf{v} , so that the final ATI quantum state is indeed well characterized by the pure state given in Eq. (E1). Therefore, the obtained results would correspond to an experimental setting where we are able to measure the kinetic energy and direction of the generated photoelectrons, and discard the results whenever the measured kinetic energy and direction are different from those of \mathbf{v} . This can be achieved by using the ATI photoelectron signal recorded by means of a time-of-flight electron spectrometer (see Fig. 10).

In particular, and with the main purpose of obtaining analytical expressions, we will restrict this analysis to time intervals for which the applied strong field is constant, that is, $f(t') = 1$ in Eq. (A4) for $t' \in [t_0, t]$. This implies that the amount of photons absorbed every half-cycle of the field would be the same, in opposition to Fig. 1(b) in the main text, where the absorption varies every half-cycle due to the modulation of the applied pulse. In practice, this would correspond to a situation where the laser source is a “long” IR pulse, meaning that we can find several cycles with almost the same peak strength on its central part. Thus, and as a first step,

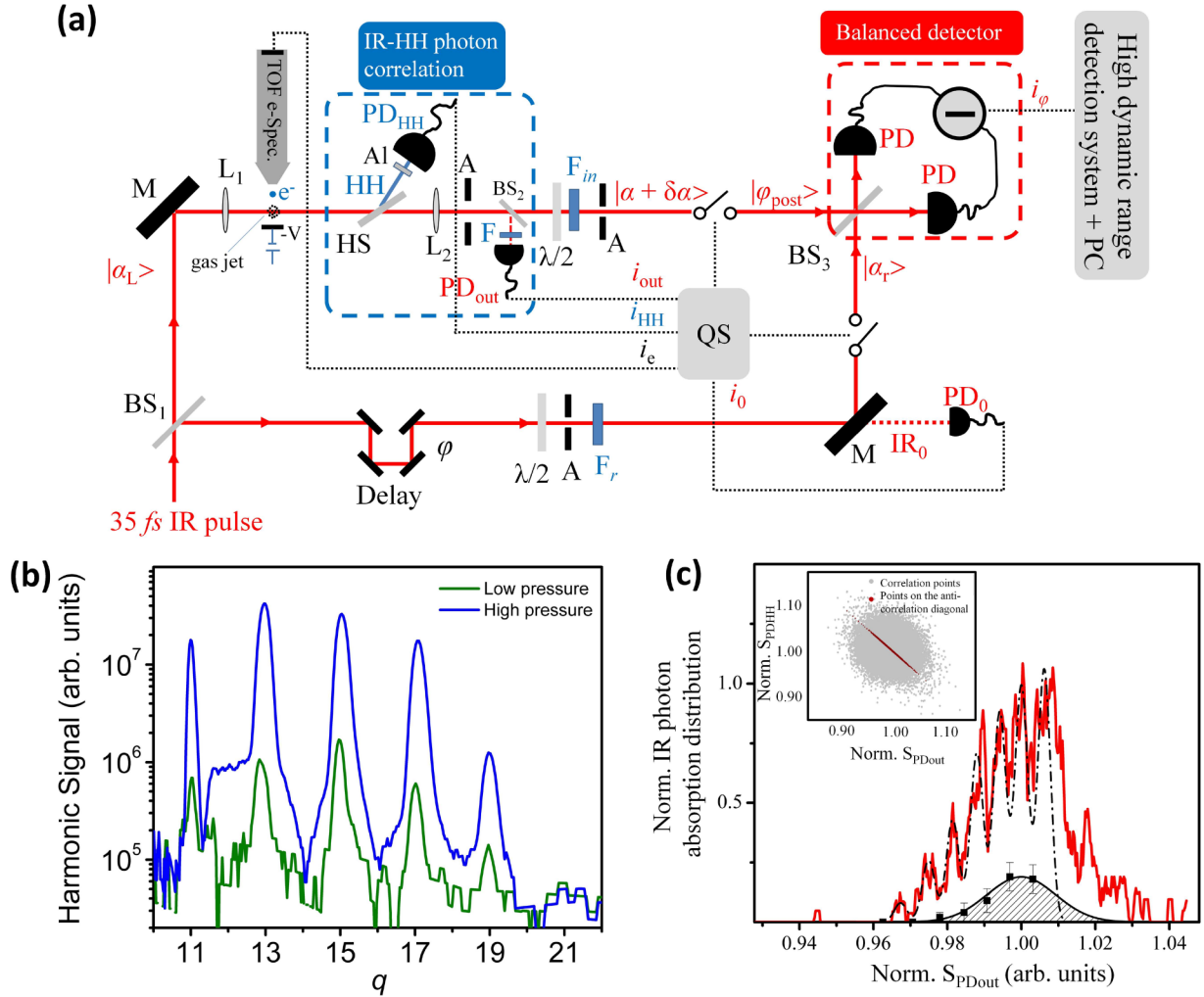


FIG. 10. Operation principle of the experimental approach. (a) Experimental setup. BS_1 : IR beam separator. $|\alpha_L\rangle$: coherent-state of IR beam passing through BS_1 . $|\alpha_r\rangle$: coherent-state IR beam reflected by BS_1 . M : IR plane mirrors. $L_{1,2}$: lens. HS : harmonic separator which reflects the high harmonics and lets the IR beam pass through. HH : high harmonics. $BS_{2,3}$: IR beam separator and splitter, respectively. PD , PD_0 , PD_{out} , PD_{HH} : IR and HH photodetectors. TOF e-Spec.: μ -metal shielded time-of-flight spectrometer that could be used for the measurement of the ATI electrons. The voltage (V) can serve for the energy selection of the electrons reaching the TOF detector. These were used by the QS in order to condition the $|\alpha_L + \delta\alpha_L\rangle$ state on the HHG process. i_ϕ , i_{out} , i_0 , i_{HH} are the photocurrent values recorded for each laser shot. These were used by the QS in order to condition the $|\alpha_L + \delta\alpha_L\rangle$ state on the HHG process. i_e is the signal of the TOF spectrometer that could be used by QS for conditioning on ATI process. Just before PD_{HH} , a 150-nm-thick aluminum filter was placed (not shown) in order to select the harmonics with $q \geq 11$. IR_0 : IR beam used to measure the shot energy of the driving field. $\lambda/2$: half-IR-wave plates. A : apertures. F , F_{in} : Neutral density filters of approximately the same transmission. F_r : neutral density filters used to control the energy of the reference coherent state of the laser field E_r . $|\alpha + \delta\alpha\rangle$: IR state after the attenuation. All signals were recorded by a high dynamics range boxcar integrator and saved/analyzed by computer (PC) software. $|\Phi_{post}\rangle$ is the quantum state of field entering the balance detector after conditioning on HHG, and E_{in} is the corresponding electric field. $|\alpha_r\rangle$ is the reference coherent state of the laser used by the QT method, and E_r is the corresponding electric field. φ : the controllable phase shift introduced in the reference beam. (b) HHG spectra measured for two different xenon gas densities in the interaction region. The blue and green lines show the harmonics recorded at high and low gas densities that have been used for the generation of the optical cat and kitten states shown in Figs. 7(b) and 7(c) of the main text of the manuscript. The harmonic signal at low gas densities is about 25 times lower than the harmonic signal recorded at high gas densities. (c) Probability of absorbing IR photons toward the harmonic generation (red line). The multipeak structure reflects the spectrum of the emitted harmonics as is described in Appendix D and Refs. [50,57,66]. The black dashed-dotted curve is the best fit of an analytical function given by the sum of a sequence of Gaussian functions. The black shaded area shows the background distribution that resulted by fitting a Gaussian function on the data (black squares) obtained by subtracting the minima of the raw data from the minima of the black dashed-dot fit. The inset shows the joint XUV-vs-IR photon number distribution using the signal of i_{HH} ($S_{PD_{HH}}$) and i_{out} ($S_{PD_{out}}$) (gray points). The red points show the selected points along the anticorrelation diagonal. The distribution was created by keeping the energy stability of the driving field at the level of $\approx 1\%$, and after subtracting the electronic noise from each laser shot.

we will rewrite Eq. (E1) as a sum of integrals defined for every half-cycle of the field

$$|\Phi(\mathbf{v}, t)\rangle = \frac{i}{\hbar} \sum_{j=0}^{\mathcal{N}-1} \int_{t_j}^{t_{j+1}} dt' \hat{\mathbf{E}}_Q(t') \cdot \mathbf{d}_H^*(\mathbf{v}, t') \times |\delta\alpha(t')\rangle \bigotimes_{q=2}^{\text{cutoff}} |\beta_q(t')\rangle, \quad (\text{E4})$$

where \mathcal{N} is the total number of half-cycles, and we identify $t_{\mathcal{N}} = t$. Note that the conditioning over a single value of direction and kinetic momentum \mathbf{v} leads to an entangled state between all the modes participating in the process. Hereupon, and in order to study the final state obtained for the IR, we will assume that during the ATI process the harmonic coherent-state amplitudes β_q stay very close to the vacuum. Thus, if under this assumption we project Eq. (E4) over the vacuum state for the harmonics, we can approximate our state by

$$|\tilde{\Phi}(\mathbf{v}, t)\rangle \approx \frac{i}{\hbar} \sum_{j=0}^{\mathcal{N}-1} \int_{t_j}^{t_{j+1}} dt' \hat{\mathbf{E}}_L(t') \cdot \mathbf{d}_H^*(\mathbf{v}, t') |\delta\alpha(t')\rangle, \quad (\text{E5})$$

where $|\tilde{\Phi}(t)\rangle = \langle 0_q | \bigotimes_q |\Phi(\mathbf{v}, t)\rangle$, and $\hat{\mathbf{E}}_L$ is the electric field operator acting over the fundamental mode, i.e., the first term of Eq. (A7).

Furthermore, under the ‘‘long’’ IR pulse considerations, the amount of photons absorbed every half-cycle is the same, that is, $\delta\alpha(t_{j+1}) - \delta\alpha(t_j) = \Delta$. This motivates us to consider a discretization of the values of $\delta\alpha(t)$ appearing on each term of the sum in Eq. (E5), such that the value of $\delta\alpha(t)$ in each integral term adopts the value of the coherent state obtained at the end of the cycle, that is,

$$|\tilde{\Phi}(\mathbf{v}, t)\rangle \approx \frac{i}{\hbar} \sum_{j=0}^{\mathcal{N}-1} \int_{t_j}^{t_{j+1}} dt' \hat{\mathbf{E}}_L(t') \cdot \mathbf{d}_H^*(\mathbf{v}, t') |(j+1)\Delta\rangle. \quad (\text{E6})$$

Of course, this approximation is not always valid. One has to guarantee that two consecutive states $|j\Delta\rangle$ and $|(j+1)\Delta\rangle$ are comparable to each other. Otherwise, smaller steps have to be considered in the discretization, which may not allow us to write the shift Δ as a time-independent quantity. A natural way of establishing such a comparison is in terms of the overlap between these two states, i.e.,

$$\langle j\Delta | (j+1)\Delta \rangle = \exp\left[-\frac{|\Delta|^2}{2}\right]. \quad (\text{E7})$$

Thus, we will restrict to values of $|\Delta| < 0.95$, for which the overlap between these two coherent states is bigger than $1 - e^{-1}$. Under these considerations, the state obtained in Eq. (E6) is given as a superposition of different coherent states, where each of them is affected by the electric field operator evaluated at time t' . Apart from this, one of the main differences of this state with respect to the one obtained through HHG, in Eq. (D2), is that in the former more than two coherent states intervene in the final superposition, depending on the number of half-cycles \mathcal{N} .

In Eq. (E6), each of these coherent states is weighted by the quantum optical version of the ATI spectrum taken at

every half-cycle of the field. This can be seen more clearly if, assuming a linearly polarized field, we substitute Eq. (A4) with the considered approximations in Eq. (E6),

$$|\phi(\mathbf{v}, t)\rangle \approx \hbar \mathbf{g}(\omega_L) \sum_{j=0}^{\mathcal{N}-1} \left(\int_{t_j}^{t_{j+1}} dt' \mathbf{d}_H^*(\mathbf{v}, t') e^{i\omega t'} \hat{a} - \mathbf{d}_H^*(\mathbf{v}, t') e^{-i\omega t'} \hat{a}^\dagger \right) |(j+1)\Delta\rangle, \quad (\text{E8})$$

where

$$\mathbf{d}_H^*(\mathbf{v}, t) = \langle \psi_{\text{sc}}(t) | e^{\hat{X}} U_{\text{sc}}(t) | \mathbf{v} \rangle = \langle \psi_{\text{sc}}(t) | e^{\hat{X}} U_{\text{sc}}(t) \left| \mathbf{p} - \frac{e}{c} \mathbf{A}_L(t_0) \right\rangle. \quad (\text{E9})$$

In this last expression, \hat{X} is the position coordinate operator affecting the electron, $\hat{U}_{\text{sc}}(t)$ is the time evolution operator of the semiclassical Hamiltonian appearing in Eq. (A11), and $|\psi_{\text{sc}}(t)\rangle = U_{\text{sc}}(t) | \mathbf{g} \rangle$ is the ground state of the electron evolved with the previous propagator. Furthermore, we have conditioned over kinetic energies that satisfy $\mathbf{v} = \mathbf{p} - (e/c)\mathbf{A}_L(t_0)$. Under the strong field assumptions, we can write the previous matrix element as

$$\mathbf{d}_H^*(\mathbf{v}, t) = \langle \psi_{\text{sc}}(t) | e^{\hat{X}} \left| \mathbf{p} - \frac{e}{c} \mathbf{A}_L(t) \right\rangle \times e^{-i[S(\mathbf{p}, t, t_0) - I_p(t - t_0)]}, \quad (\text{E10})$$

with $S(\mathbf{p}, t, t_0)$ the semiclassical action given in Eq. (B23). By expanding this expression using the form of $|\psi_{\text{sc}}(t)\rangle$ given by the semiclassical analysis [22], one can see that this term can be written as the sum of two terms characterizing direct ionization phenomena and rescattering processes [78]. In our case, we are only interested in direct ionization processes, so we restrict our calculations to values of the electron kinetic energy lower than $2U_p$, with U_p the ponderomotive potential. Thus, we write this matrix element as

$$\mathbf{d}_H^*(\mathbf{v}, t) \approx \langle \mathbf{g} | e^{\hat{X}} \left| \mathbf{p} - \frac{e}{c} \mathbf{A}_L(t) \right\rangle e^{-i[S(\mathbf{p}, t, t_0) - I_p t]}. \quad (\text{E11})$$

Now, we explicitly compute the expression for the Wigner function of the state in Eq. (E6). With that purpose, let us first define the quantities A_j and B_j as

$$A_j = \frac{1}{\hbar} \mathbf{g}(\omega_L) \int_{t_j}^{t_{j+1}} dt' \mathbf{d}_H^*(\mathbf{v}, t') e^{i\omega t'}, \quad (\text{E12})$$

$$B_j = \frac{1}{\hbar} \mathbf{g}(\omega_L) \int_{t_j}^{t_{j+1}} dt' \mathbf{d}_H^*(\mathbf{v}, t') e^{-i\omega t'},$$

where $\mathbf{d}_H^*(\mathbf{v}, t)$ is given as in Eq. (E11), such that the state in Eq. (E6) can be written as

$$|\tilde{\Phi}(\mathbf{v}, t)\rangle = i \sum_{j=0}^{\mathcal{N}-1} (A_j \hat{a} - B_j \hat{a}^\dagger) |(j+1)\Delta\rangle. \quad (\text{E13})$$

Introducing here the definition of the photonic quadrature operators, \hat{x}_L and \hat{p}_L given in the main text, we can rewrite the

previous state as

$$|\tilde{\Phi}(\mathbf{v}, t)\rangle = i \sum_{j=0}^{\mathcal{N}-1} (C_j^{(-)} \hat{x}_L + iC_j^{(+)} \hat{p}_L) |(j+1)\Delta\rangle, \quad (\text{E14})$$

where $C_j^{\pm} = (1/\sqrt{2})(A_j \pm B_j)$. Thus, for computing the Wigner function by means of

$$W(x, p) = \frac{1}{\pi \hbar} \int_{-\infty}^{\infty} \langle x+y | \tilde{\rho}_{\text{ATI-IR}} | x-y \rangle e^{-i2py/\hbar}, \quad (\text{E15})$$

we first give an expression for the matrix element of $\rho = |\tilde{\Phi}(\mathbf{v}, t)\rangle \langle \tilde{\Phi}(\mathbf{v}, t)|$ between two different position states $|x \pm y\rangle$,

$$\begin{aligned} \langle x+y | \rho | x-y \rangle &= \left[\sum_{j=0}^{\mathcal{N}-1} C_j^{(+)} \langle x+y | \hat{x}_L | (j+1)\Delta \rangle \right. \\ &\quad \left. + iC_j^{(-)} \langle x+y | \hat{p}_L | (j+1)\Delta \rangle \right] \\ &\times \left[\sum_{k=0}^{\mathcal{N}-1} C_k^{(+)*} \langle (k+1)\Delta | \hat{x}_L | x-y \rangle \right. \\ &\quad \left. - iC_k^{(-)*} \langle (k+1)\Delta | \hat{p}_L | x-y \rangle \right], \quad (\text{E16}) \end{aligned}$$

with

$$\begin{aligned} \langle x+y | \hat{x}_L | (j+1)\Delta \rangle &= (x+y)G_{+,j}, \\ \langle x+y | \hat{p}_L | (j+1)\Delta \rangle &= -i \frac{\partial G_{+,j}}{\partial(x+y)}, \end{aligned} \quad (\text{E17})$$

where the functions $G_{\pm,j} = \langle x \pm y | (j+1)\Delta \rangle$ are given by

$$\langle x | \alpha \rangle = \frac{1}{\pi^{1/4}} \exp\left[-\frac{[x - \sqrt{2} \text{Re}(\alpha)]^2}{2} + ix\sqrt{2} \text{Im}(\alpha)\right]. \quad (\text{E18})$$

With all this, the matrix element in Eq. (E16) reads

$$\begin{aligned} \langle x+y | \rho | x-y \rangle &= \sum_{j,k}^{\mathcal{N}-1} \left[C_j^{(-)} C_k^{(-)*} (x^2 - y^2) G_{+,j} G_{-,k}^* \right. \\ &\quad + C_j^{(+)} C_k^{(+)*} \frac{\partial G_{+,j}}{\partial(x+y)} \frac{\partial G_{-,k}^*}{\partial(x-y)} \\ &\quad + C_j^{(-)} C_k^{(+)*} (x+y) G_{+,j} \frac{\partial G_{-,k}^*}{\partial(x-y)} \\ &\quad \left. + C_j^{(+)} C_k^{(-)*} (x-y) \frac{\partial G_{+,j}}{\partial(x+y)} G_{-,k}^* \right], \quad (\text{E19}) \end{aligned}$$

and thus the Wigner function can be computed by introducing this expression for the matrix element inside Eq. (E15). Note that this expression will only contain derivatives involving Gaussian functions, so it can be computed analytically. In particular, we have performed these calculations in atomic units ($\hbar = 1$, $e^2 = 1$, $m_e = 1$, and $k_c = 1/4\pi\epsilon_0 = 1$). In particular, we considered the ionization potential of a hydrogen atom $I_p = 0.5$ a.u., the frequency for the fundamental mode

$\omega = 0.057$ a.u., and the amplitude of the electromagnetic field $E_L = 0.053$ a.u.

2. ATI state conditioned over all possible outgoing momenta

The density matrix that characterizes the total IR ATI state involving all the possible momenta for the generated photoelectrons is

$$\begin{aligned} \rho_{\text{ATI}} &= \int d\mathbf{v} |\Phi(\mathbf{v}, t)\rangle \langle \Phi(\mathbf{v}, t)| \Phi(\mathbf{v}, t) \\ &= \int d\mathbf{v} \int_{t_0}^t dt' \int_{t_0}^t dt'' \hat{\mathbf{E}}_Q(t') \cdot \mathbf{d}_H^*(\mathbf{v}, t') \\ &\quad \times |\Phi(t')\rangle \langle \Phi(t')| \Phi(t'') \mathbf{d}_H(\mathbf{v}, t'') \cdot \hat{\mathbf{E}}_Q(t''), \quad (\text{E20}) \end{aligned}$$

which, taking into account the SFA version of the identity, i.e.,

$$\mathbb{1} \approx |\mathbf{g}\rangle \langle \mathbf{g}| + \int d\mathbf{v} |\mathbf{v}\rangle \langle \mathbf{v}|, \quad (\text{E21})$$

and considering for simplicity a linearly polarized light, can be rewritten as

$$\begin{aligned} \rho_{\text{ATI}} &= \int_{t_0}^t dt' \int_{t_0}^t dt'' \hat{E}_Q(t') |\Phi(t')\rangle \langle \Phi(t')| \Phi(t'') \hat{E}_Q(t'') \\ &\quad \times [\langle \hat{d}_H(t') \hat{d}_H(t'') \rangle - d_H(t') d_H(t'')], \quad (\text{E22}) \end{aligned}$$

where the term between brackets contains the difference between the correlation of the dipole operator at times t' and t'' , and the product of the mean values of such operators at the corresponding times, both terms evaluated with respect to the ground state of the system. For other possible field polarizations, the expression adopts the same form but we would have to consider contributions coming from the different polarization terms for the term between brackets. Obviously, while measurement conditioned on all electrons should be easier, the theoretical analysis is tougher as it requires evaluation of the two-time correlation functions of the dipole moment. This can be done, in principle, using SFA or even TDSE, but it leads to much more complicated expressions, which will be analyzed elsewhere [79].

To gain intuition about the IR ATI state obtained from Eq. (E22), we are going to work within the same approximations that lead to Eq. (E5), and considering the simplifying assumption that all the generated coherent shifts are identical and time-independent. In general this is not true, and as discussed in Fig. 1 in the main text, the coherent shift is continuously increasing along the pulse. However, for single-photon ionization processes one may expect this shift to be very small and, in some sense, indistinguishable from all the other values it can take along the whole pulse duration. Therefore, under this consideration the ATI state reads

$$\begin{aligned} \tilde{\rho}_{\text{ATI-IR}} &= \int_{t_0}^t dt' \int_{t_0}^t dt'' \hat{E}_L(t') |\delta\alpha\rangle \langle \delta\alpha| \hat{E}_L(t'') \\ &\quad \times K(t', t'') e^{i\varphi(t')} e^{-i\varphi(t'')}, \quad (\text{E23}) \end{aligned}$$

where $K(t', t'') = \langle \hat{d}_H(t') \hat{d}_H(t'') \rangle - d_H(t') d_H(t'')$, and the exponential terms are the factors coming from the BCH formula, which we have to explicitly consider as they cannot be factorized now. Furthermore, if we introduce here the definition of

part of the electric field operator that acts over the fundamental mode [first term in Eq. (A4)], we get

$$\begin{aligned} \tilde{\rho}_{\text{ATI-IR}} &= \hbar^2 |\mathbf{g}(\omega_L) \cdot \boldsymbol{\epsilon}_{\mu,L}|^2 \int_{t_0}^t dt' \int_{t_0}^{t'} dt'' K(t', t'') \\ &\times [\hat{a}^\dagger |\delta\alpha\rangle \langle \delta\alpha| \hat{a}^\dagger e^{i\omega_L(t'+t'')} + \hat{a} |\delta\alpha\rangle \langle \delta\alpha| \hat{a} e^{-i\omega_L(t'+t'')} \\ &- \hat{a}^\dagger |\delta\alpha\rangle \langle \delta\alpha| \hat{a} e^{i\omega_L(t'-t'')} - \hat{a} |\delta\alpha\rangle \langle \delta\alpha| \hat{a}^\dagger e^{-i\omega_L(t'-t'')}], \end{aligned} \quad (\text{E24})$$

Thus, one of the main advantages of the previous approximation is that the temporal part only affects the coefficients of the obtained mixed state. This allows us to write Eq. (E22) as

$$\begin{aligned} \tilde{\rho}_{\text{ATI-IR}} &= -i\hbar |\mathbf{g}(\omega_L) \cdot \boldsymbol{\epsilon}_{\mu,L}| \\ &\times [I_1(t) \hat{a}^\dagger |\delta\alpha\rangle \langle \delta\alpha| \hat{a}^\dagger + I_2(t) \hat{a} |\delta\alpha\rangle \langle \delta\alpha| \hat{a} \\ &- I_3(t) \hat{a}^\dagger |\delta\alpha\rangle \langle \delta\alpha| \hat{a} - I_4(t) \hat{a} |\delta\alpha\rangle \langle \delta\alpha| \hat{a}^\dagger], \end{aligned} \quad (\text{E25})$$

where we have defined

$$I_1(t) = \int_{t_0}^t dt' \int_{t_0}^{t'} dt'' \bar{K}(t', t'') e^{i\omega_L(t'+t'')}, \quad (\text{E26})$$

$$I_2(t) = \int_{t_0}^t dt' \int_{t_0}^{t'} dt'' \bar{K}(t', t'') e^{-i\omega_L(t'+t'')}, \quad (\text{E27})$$

$$I_3(t) = \int_{t_0}^t dt' \int_{t_0}^{t'} dt'' \bar{K}(t', t'') e^{i\omega_L(t'-t'')}, \quad (\text{E28})$$

$$I_4(t) = \int_{t_0}^t dt' \int_{t_0}^{t'} dt'' \bar{K}(t', t'') e^{-i\omega_L(t'-t'')}, \quad (\text{E29})$$

with $\bar{K}(t', t'') = K(t', t'') e^{i\varphi(t')} e^{-i\varphi(t'')}$.

The dipole correlator $K(t', t'')$ is difficult to compute, since it is not a quantity that can be obtained directly from the numerical implementations of the TDSE, nor from a SFA analysis. Thus, the approach we consider here in order to gain intuition about what to expect from the obtained Wigner functions is to look for some relations between the $I_i(t)$ coefficients so that we can bring Eq. (E25) to a very simplified form, and then study different limits regarding the coefficients. First of all, we note that the $\bar{K}(t', t'')$ satisfies $\bar{K}(t', t'') = \bar{K}^*(t'', t')$, which allows us to conclude after some algebraic operations that $I_1(t) = I_2^*(t)$ and that $I_3(t)$ and $I_4(t)$ are real functions.

The above relations allow us to further simplify the final form of $\tilde{\rho}_{\text{ATI-IR}}$, and they provide us with the final form we use for the Wigner function computation,

$$\begin{aligned} \tilde{\rho}_{\text{ATI-IR}} &= -i\hbar |\mathbf{g}(\omega_L) \cdot \boldsymbol{\epsilon}_{\mu,L}| \\ &\times [I_1(t) \hat{a}^\dagger |\delta\alpha\rangle \langle \delta\alpha| \hat{a}^\dagger + I_1^*(t) \hat{a} |\delta\alpha\rangle \langle \delta\alpha| \hat{a} \\ &- I_3(t) \hat{a}^\dagger |\delta\alpha\rangle \langle \delta\alpha| \hat{a} - I_4(t) \hat{a} |\delta\alpha\rangle \langle \delta\alpha| \hat{a}^\dagger]. \end{aligned} \quad (\text{E30})$$

Then, using the definition of the Wigner function given in [77], we get for our state

$$\begin{aligned} W(\beta) &= \frac{2}{\pi N} e^{-\frac{1}{2}|2\beta - \delta\alpha|} \\ &\times [I_1(t) \delta\alpha(2\beta - \delta\alpha) + I_1^*(t) \delta\alpha^*(2\beta - \delta\alpha)^* \\ &- I_3(t) |\delta\alpha| - I_4(t) (|2\beta - \delta\alpha| - 1)], \end{aligned} \quad (\text{E31})$$

where N is a normalization constant. As was mentioned before, the computation of the $K(t, t')$ function is not trivial

at all, and in the strong-field community it is common to approximate the absolute value of the Fourier transform of the dipole-dipole correlator with the absolute value of the Fourier transform given by the dipole, i.e., the fundamental component of the HHG spectrum (cf. [80]). In our case, and to gain insight about the form of the final Wigner function, we neglect the effect of the exponentials with respect to $(t' + t'')$ as we expect their contribution to be lower than the ones provided by $(t' - t'')$, as their oscillation is faster. With this, one can check that for different values of the weights provided by the integrals $I_3(t)$ and $I_4(t)$, the final Wigner function presents a similar behavior to that obtained in HHG. Because of the form of the considered quantum state, this is something we should expect since $\hat{E}_L(t) |\delta\alpha\rangle \propto |\delta\alpha\rangle$ when $\delta\alpha$ adopts very large values.

APPENDIX F: OPERATION PRINCIPLE OF THE EXPERIMENTAL APPROACH

An optical layout of the system is shown in Fig. 10(a). Although the system can be implemented for conditioning on HHG and/or ATI processes, here we will show its applicability using the HHG process induced by the interaction of the fundamental driving field with Xe gas. The approach has been also discussed in Ref. [50]. The experiment was performed using a linearly polarized ≈ 35 fs Ti:sapphire laser pulse of $\lambda \approx 800$ nm carrier wavelength and an interferometer. The whole system was operating at 0.5 kHz repetition rate. The IR laser beam was separated into the branches of the interferometer by a beam separator BS_1 . The IR beam reflected by the BS_1 (in the second branch of the interferometer) serves as a reference beam of the quantum tomography (QT) method and for measuring (by means of IR photodiode PD_0) the shot-to-shot energy fluctuations of the driving field. In the first branch of the interferometer, the IR beam was focused by means of a 15 cm focal length lens (L_1) into a xenon pulsed gas jet, where the HHG process takes place. In the present experiment, the optimum intensity of the IR pulse in the interaction region resulting in a maximum harmonic order was $\approx 8 \times 10^{13}$ W/cm², while the maximum harmonic yield was observed for a gas density in the order $\sim 10^{18}$ atoms/cm³. The generated harmonics, after a reflection by a multilayer infrared-antireflection coating plane mirror (HS) placed at grazing incidence angle, was passing through a 150-nm-thick aluminum filter, which selects all the harmonics with $q \geq 11$ [Fig. 10(b)]. The photon number of the XUV radiation was measured by means of a calibrated XUV detector PD_{HH} . A portion of the IR field exiting the xenon gas was reflected by the IR beam separator BS_2 toward IR photodiode PD_{out} (operating in the linear regime) placed after a lens [used to collect the photons on the surface of the diode, not shown in Fig. 10(a)] and a neutral density filter (F) which significantly reduces the photon number and ensures the avoidably of saturation effects. The photocurrent signals i_{HH} , i_0 , i_{out} of PD_{HH} , PD_0 , and PD_{out} were used by the quantum spectrometer (QS) to disentangle the high harmonic generation process from all other processes induced by the interaction. The IR field after BS_2 was collimated by a planoconvex lens (L_2) while the mean photon number of the IR field (E_{in}), before reaching the balanced detector of the QT, was reduced (by

means of neutral density filters F_{in}) to the level of a few photons per pulse, with the QS to select, for each laser shot, only the IR photons related to the HHG. The QS approach [57,66] relies on shot-to-shot correlation between the photon number of the generated harmonics (integrated signal of $q \geq 11$) and the IR field exiting the medium [gray points in the inset of Fig. 10(c)]. The conditioning to HHG is achieved by selecting only the shots that provide a signal along the anticorrelation diagonal of the joint distribution [red points in the inset Fig. 10(c)]. By selecting these points, we collect only the shots that are relevant to the harmonic emission, and we remove the unwanted background associated with all processes irrelevant to the harmonic generation. In this way, we obtain the probability of absorbing IR photons towards the harmonic generation [red line in Fig. 10(c)]. The IR absorption probability distribution consists in a multipeak structure that corresponds to the harmonic order [57,66]. The black line in Fig. 10(c) shows the remaining background distribution, which has been subtracted from the data, as it is related only with the ability of the present QS experimental apparatus to remove all the shots associated with processes irrelevant to the HHG process (for details, see Refs. [50,57,75]).

The E_{in} field was spatiotemporally overlapped on a beam splitter (BS_2) with a local oscillator laser field (E_r), unaffected by the interaction, coming from the second branch of the interferometer, which consists of a piezobased delay stage that introduces a controllable delay $\Delta\tau$ (phase shift φ) between the E_r and E_{in} fields. The interfering fields outgoing from the BS_2 were detected by the diodes (PD) of a high bandwidth (from DC to 350 MHz), high subtraction efficiency, and high quantum efficiency balanced amplified differential photodetector, which provides at each value of φ the signal difference. The photocurrent difference i_φ , as well as the photocurrent values of the IR and HH detectors (i_{out} , i_0 , i_{HH}) in the QS, were simultaneously recorded for each laser shot by a multichannel 16-bit high dynamic range boxcar integrator. For each shot, the background electronic noise was recorded and subtracted by the corresponding photocurrent signal by placing a second time-gate in the boxcar integrator in times significantly delayed compared to the arrival times of the photon signals. Setting the delay stage around $\Delta\tau \approx 0$, the characterization of the quantum state of light was achieved by recording for each shot the value of i_φ as a function of φ , by moving the piezo from $\varphi \approx 0$ to $\varphi \approx \pi$. The homodyne data were scaled according to the measured vacuum state quadrature noise.

APPENDIX G: RECONSTRUCTION OF THE WIGNER FUNCTION

The values of the photocurrent difference i_φ are directly proportional to the measurement of the electric field operator $\hat{E}_{\text{in}}(\varphi) \propto \hat{x}_\varphi = \cos(\varphi)\hat{x} + \sin(\varphi)\hat{p}$, and have been used for the reconstruction of the Wigner function. When the xenon gas jet and the QS are switched on, the homodyne detection system provides the measurement \hat{x}_φ only when the IR field exiting the atomic medium is conditioned on the HHG, leading to the characterization of the light state $|\Phi_{\text{post}}\rangle = |\alpha_L + \delta\alpha_L\rangle - \xi|\alpha_L\rangle$. Repeated measurements of \hat{x}_φ at each φ provide the probability distribution $P_\varphi(x_\varphi) = \langle x_\varphi | \hat{\rho} | x_\varphi \rangle$ of its eigenvalues x_φ (where $\hat{\rho} \equiv |\Phi_{\text{post}}\rangle\langle\Phi_{\text{post}}|$ is the density operator of the

light state and $|x_\varphi\rangle$ is the eigenstate with eigenvalue x_φ). For each data set in the range of $0 < \varphi < \pi$ around $\Delta\tau \approx 0$, the Wigner function was reconstructed by means of the inverse radon transformation implemented via the standard filtered backprojection algorithm [55,56]. The algorithm used to reconstruct the Wigner functions was applied directly to the quadrature values $x_{\varphi,k}$, where k is the index of each value, using the formula [55,56] $W(x, p) \simeq \frac{1}{2\pi^2 N} \sum_{k=1}^N K[x \cos(\varphi_k) + p \sin(\varphi_k) - x_{\varphi,k}]$. $K(z) = \frac{1}{2} \int_{-\infty}^{\infty} |\xi| \exp(i\xi z) d\xi$ is called the integration kernel with $z = x \cos(\varphi_k) + p \sin(\varphi_k) - x_{\varphi,k}$. The numerical implementation of the integration kernel requires the replacement of the infinite integration limits with a finite cutoff frequency k_c . To reduce the numerical artifacts (rapid oscillations) and allow the details of the Wigner function to be resolved, the value of k_c was set to ≈ 3.7 for all measurements presented here. An estimation of the error of the reconstructed $W(x, p)$ has been obtained by comparing (subtracting) the ideal Wigner function of a coherent state from the Wigner function of a coherent state reconstructed by the experimental data. The deviation from the ideal case provides an error of ± 0.004 in $W(x, p)$. The accuracy of measuring the photon number was in the range of $\approx 1.5\%$ to $\approx 3.5\%$ of the mean for high and low photon numbers, respectively. This was obtained following the aforementioned procedure using the density matrices ρ_{nm} in Fock space (n, m). The mean photon number was obtained by the diagonal elements ρ_{nn} of the ρ_{nm} and the relation $\langle n \rangle = \sum n \rho_{nn}$.

APPENDIX H: ERROR ANALYSIS OF THE RECONSTRUCTED WIGNER FUNCTION AND THE PHOTON NUMBER

The numerical implementation of the integration kernel for the reconstruction of the Wigner function requires the replacement of the infinite integration limits with a finite cutoff frequency k_c . To reduce the numerical artifacts (rapid oscillations) and allow the details of the Wigner function to be resolved, the value of k_c was set to ≈ 3.7 for all measurements presented here. An estimation of the error of the reconstructed $W(x, p)$ has been obtained by comparing (subtracting) the ideal Wigner function of a coherent state from the Wigner function of a coherent state reconstructed by the experimental data. This is shown in Fig. 11(a) as a function of k_c . The deviation from the ideal case provides an error $\approx 1.5\%$ resulting in an error of ± 0.004 in the $W(x, p)$ shown in the main text. This figure also shows that the value of $k_c \approx 3.7$ is indeed the optimum one.

To obtain the accuracy of measuring the photon number, we have followed the aforementioned procedure for each light state shown in the main text, using the density matrices ρ_{nm} in Fock space (n, m). The mean photon number was obtained by the diagonal elements ρ_{nn} of the ρ_{nm} and the relation $\langle n \rangle = \sum n \rho_{nn}$. The results shown in Fig. 11(b) have been obtained by calculating the mean photon number value ($\langle n_{\text{rec}} \rangle$) of a coherent state numerically constructed using the number of data points recorded in the experiment. This value has been compared with the value resulting from the ideal theoretical case ($\langle n_{\text{th}} \rangle$), i.e., we obtain [$\langle n \rangle$ Error (%)] = $|\langle n_{\text{rec}} \rangle - \langle n_{\text{th}} \rangle| / \langle n_{\text{th}} \rangle$. This procedure has been repeated for

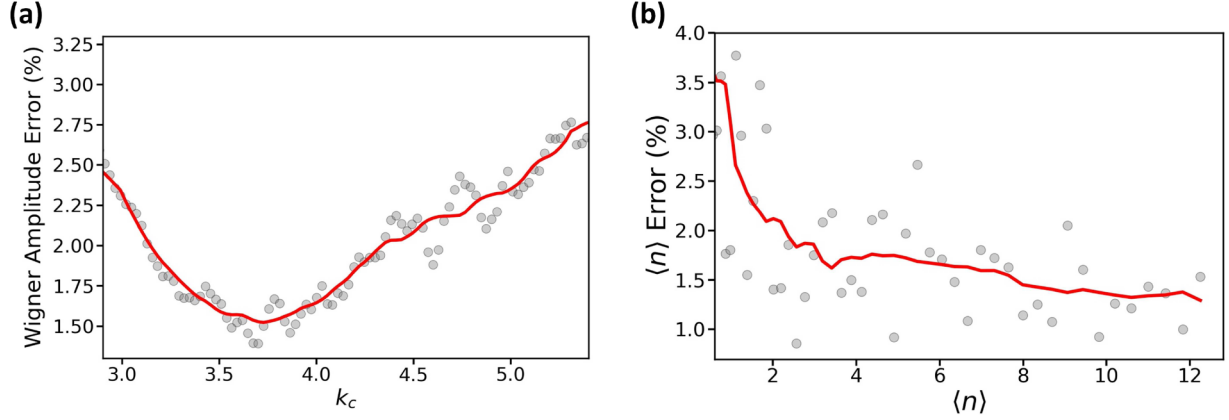


FIG. 11. Error analysis of the reconstructed Wigner function and the photon number. (a) Dependence of the error of the Wigner function reconstructed by the experimental data on k_c . (b) Dependence of accuracy of measuring the photon number on the mean photon number of the light state. In both graphs, the red solid line is a 15-points running average of the data (gray points).

different photon number values of the coherent state. It is found that the accuracy of measuring the photon number is in the range of $\approx 1.5\%$ to $\approx 3.5\%$ of the mean, for high and low photon numbers, respectively.

APPENDIX I: AB INITIO ANALYSIS OF THE DECOHERENCE DUE TO THE INTERACTION WITH AN ENVIRONMENT

Here, we further extend our calculations to the interaction of the obtained HHG Schrödinger optical cat states with an environment. In particular, the model we consider is that of a beam splitter, where in one of the input modes we introduce the quantum state we want to study, and on the other an ancillary vacuum state that is traced out at the output. Thus, we can understand this ancillary mode as the part of the field that is absorbed by the environment. Although simple, this model has been proven to be exact when describing interactions with a Gaussian reservoir [68], and we show here that it describes the differences obtained between the theoretical and experimental Wigner functions.

According to this model, the state after the interaction with the environment is described by

$$\tilde{\rho} = \text{tr}_{\text{anc}}(B(\theta)|\Phi_{\text{post}}\rangle\langle\Phi_{\text{post}}| \otimes |0_{\text{anc}}\rangle\langle 0_{\text{anc}}|B(\theta)^\dagger), \quad (\text{I1})$$

where tr_{anc} represents the partial trace over the ancillary mode, and $B(\theta) \equiv \exp[\theta(\hat{a}\hat{a}_{\text{anc}}^\dagger - \hat{a}_{\text{anc}}^\dagger\hat{a})]$ is a unitary operator describing the beam splitter, where \hat{a}_{anc} ($\hat{a}_{\text{anc}}^\dagger$) is the annihilation (creation) operator acting over the ancillary modes, θ is a parameter related to the transmission efficiency η by $\eta = \cos(\theta)^2$, and $|\Phi_{\text{post}}\rangle$ is the HHG optical cat state given in Eq. (D2).

We find for the noise-affected state

$$\begin{aligned} \tilde{\rho} = & \frac{1}{N} [|(\alpha + \delta\alpha) \cos(\theta)\rangle\langle(\alpha + \delta\alpha) \cos(\theta)| \\ & + |\xi| |\alpha \cos(\theta)\rangle\langle\alpha \cos(\theta)| \\ & - \xi \tilde{\xi} |\alpha \cos(\theta)\rangle\langle(\alpha + \delta\alpha) \cos(\theta)| \\ & - \xi^* \tilde{\xi}^* |(\alpha + \delta\alpha) \cos(\theta)\rangle\langle\alpha \cos(\theta)|, \end{aligned} \quad (\text{I2})$$

where $\xi = \langle\alpha|\alpha + \delta\alpha\rangle$, $\tilde{\xi} = \langle\alpha \sin(\theta)|(\alpha + \delta\alpha) \sin(\theta)\rangle$, and N is the normalization factor. Using the definition for the Wigner function provided in [77], we find

$$\begin{aligned} W(\beta) = & \frac{2}{\pi N} [e^{-2|\beta - (\alpha + \delta\alpha) \cos(\theta)|} + |\xi| e^{-2|\beta - \alpha \cos(\theta)|} \\ & - (\xi \tilde{\xi} e^{-i2 \text{Im}(\beta) \delta\alpha \cos(\theta)} + \xi^* \tilde{\xi}^* e^{i2 \text{Im}(\beta) \delta\alpha \cos(\theta)}) \\ & \times e^{-\frac{1}{2}|2\beta - (2\alpha + \delta\alpha) \cos(\theta)|}, \end{aligned} \quad (\text{I3})$$

whose main features are shown in Fig. 12. In these plots, we considered $\delta\alpha = -0.8i$ and decreasing values, from (a) to (d), of the transmission efficiency. As we can see, the Wigner distributions keep their shape while the negative regions become smaller. Evidently, in the case of zero transmissivity, we get

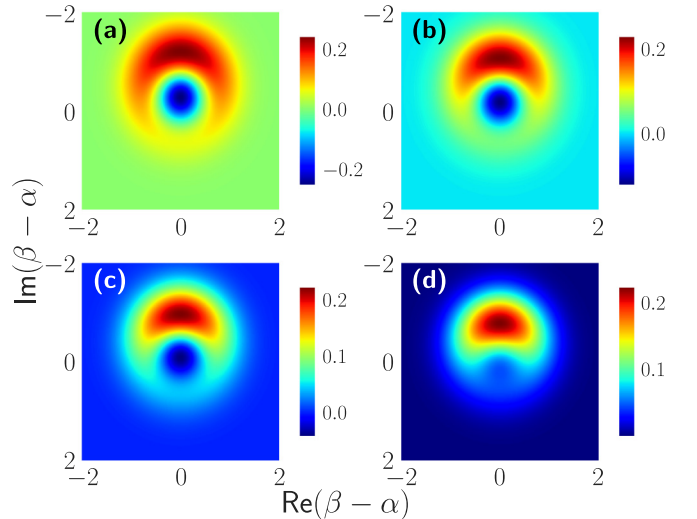


FIG. 12. Wigner functions of the cat state after considering its interaction with the environment. Here, we consider $\delta\alpha = -0.8i$ and transmission efficiencies (a) $\eta = 1.0$, (b) $\eta = 0.75$, (c) $\eta = 0.59$, and (d) $\eta = 0.39$. The different axes characterize the different quadratures of the field, in particular $\text{Re}[\beta - \alpha] \equiv x_L$, $\text{Im}[\beta - \alpha] \equiv p_L$, with x_L, p_L the values of the quadrature field operators $\hat{x}_L = (\hat{a} + \hat{a}^\dagger)/\sqrt{2}$ and $\hat{p}_L = (\hat{a} - \hat{a}^\dagger)/i\sqrt{2}$.

a Gaussian distribution that is centered in the origin. These features describe very well the experimental observations, where the negative regions become very small compared to

the theoretical values. However, in the experiment we also have the noise contributions coming from the measurement devices, which are not captured by this simple model.

-
- [1] A. Acín, I. Bloch, H. Buhrman, T. Calarco, C. Eichler, J. Eisert, D. Esteve, N. Gisin, S. J. Glaser, F. Jelezko, S. Kuhr, M. Lewenstein, M. F. Riedel, P. O. Schmidt, R. Thew, A. Wallraff, I. Walmsley, and F. K. Wilhelm, The quantum technologies roadmap: a European community view, *New J. Phys.* **20**, 080201 (2018).
- [2] I. A. Walmsley, Quantum optics: Science and technology in a new light, *Science* **348**, 525 (2015).
- [3] I. H. Deutsch, Harnessing the power of the second quantum revolution, *PRX Quantum* **1**, 020101 (2020).
- [4] W. Vogel and D.-G. Welsch, *Quantum Optics* (Wiley, Weinheim, 2006).
- [5] G. Grynberg, A. Aspect, and C. Fabre, *Introduction to Quantum Optics: From the Semi-classical Approach to Quantized Light* (Cambridge University Press, Cambridge, 2010).
- [6] W. P. Schleich, *Quantum Optics in Phase Space* (Wiley, Berlin, 2011).
- [7] A. I. Lvovsky, P. Grangier, A. Ourjoumtsev, V. Parigi, M. Sasaki, and R. Tualle-Brouri, Production and applications of non-Gaussian quantum states of light, [arXiv:2006.16985](https://arxiv.org/abs/2006.16985).
- [8] T. C. Ralph, A. Gilchrist, G. J. Milburn, W. J. Munro, and S. Glancy, Quantum computation with optical coherent states, *Phys. Rev. A* **68**, 042319 (2003).
- [9] B. C. Sanders, Entangled coherent states, *Phys. Rev. A* **45**, 6811 (1992).
- [10] H. Jeong, W. Son, M. S. Kim, D. Ahn, and Č. Brukner, Quantum nonlocality test for continuous-variable states with dichotomic observables, *Phys. Rev. A* **67**, 012106 (2003).
- [11] M. Stobińska, H. Jeong, and T. C. Ralph, Violation of Bell's inequality using classical measurements and nonlinear local operations, *Phys. Rev. A* **75**, 052105 (2007).
- [12] W. J. Munro, K. Nemoto, G. J. Milburn, and S. L. Braunstein, Weak-force detection with superposed coherent states, *Phys. Rev. A* **66**, 023819 (2002).
- [13] A. Zavatta, S. Viciani, and M. Bellini, Quantum-to-classical transition with single-photon-added coherent states of light, *Science (NY)* **306**, 660 (2004).
- [14] M. Dakna, T. Anhut, T. Opatrny, L. Knöll, and D.-G. Welsch, Generating Schrödinger-cat-like states by means of conditional measurements on a beam splitter, *Phys. Rev. A* **55**, 3184 (1997).
- [15] A. Ourjoumtsev, R. Tualle-Brouri, J. Laurat, and P. Grangier, Generating optical Schrödinger kittens for quantum information processing, *Science (NY)* **312**, 83 (2006).
- [16] A. Ourjoumtsev, H. Jeong, R. Tualle-Brouri, and P. Grangier, Generation of optical 'Schrödinger cats' from photon number states, *Nature (London)* **448**, 784 (2007).
- [17] B. Hacker, S. Welte, S. Daiss, A. Shaukat, S. Ritter, L. Li, and G. Rempe, Deterministic creation of entangled atom-light Schrödinger-cat states, *Nat. Photon.* **13**, 110 (2019).
- [18] D. V. Sychev, A. E. Ulanov, A. A. Pushkina, M. W. Richards, I. A. Fedorov, A. I. Lvovsky, Enlargement of optical Schrödinger's cat states, *Nat. Photon.* **11**, 379 (2017).
- [19] G. Mourou, Nobel Lecture: Extreme light physics and application, *Rev. Mod. Phys.* **91**, 030501 (2019).
- [20] D. Strickland, Nobel Lecture: Generating high-intensity ultrashort optical pulses, *Rev. Mod. Phys.* **91**, 030502 (2019).
- [21] P. B. Corkum, Plasma Perspective on Strong Field Multiphoton Ionization, *Phys. Rev. Lett.* **71**, 1994 (1993).
- [22] M. Lewenstein, P. Balcou, M. Y. Ivanov, A. L'Huillier, and P. B. Corkum, Theory of high-harmonic generation by low-frequency laser fields, *Phys. Rev. A* **49**, 2117 (1994).
- [23] K. Amini, J. Biegert, F. Calegari, A. Chacón, M. F. Ciappina, A. Dauphin, D. K. Efimov, C. F. d. M. Faria, K. Giergiel, P. Gniewek, A. S. Landsman, M. Lesiuk, M. Mandrysz, A. S. Maxwell, R. Moszyński, L. Ortmann, J. A. Pérez-Hernández, A. Picón, E. Pisanty, J. Prauzner-Bechcicki *et al.*, Symphony on strong field approximation, *Rep. Prog. Phys.* **82**, 116001 (2019).
- [24] K. C. Kulander, K. J. Schafer, and J. L. Krause, Dynamics of short-pulse excitation, ionization and harmonic conversion, in *Super-Intense Laser-Atom Physics*, NATO ASI Series, edited by B. Piraux, A. L'Huillier, and K. Rzażewski (Springer, Boston, 1993), pp. 95–110.
- [25] P. Salières, B. Carré, L. L. Déroff, F. Grasbon, G. G. Paulus, H. Walther, R. Kopold, W. Becker, D. B. Milošević, A. Sanpera, and M. Lewenstein, Feynman's path-integral approach for intense-laser-atom interactions, *Science* **292**, 902 (2001).
- [26] G. Vampa, T. J. Hammond, M. Taucer, X. Ding, X. Ropagnol, T. Ozaki, S. Delprat, M. Chaker, N. Thiré, B. E. Schmidt, F. Légaré, D. D. Klug, A. Y. Naumov, D. M. Villeneuve, A. Staudte, and P. B. Corkum, Strong-field optoelectronics in solids, *Nat. Photon.* **12**, 465 (2018).
- [27] M. F. Ciappina, J. A. Pérez-Hernández, A. S. Landsman, W. A. Okell, S. Zherebtsov, B. Förg, J. Schötz, L. Seiffert, T. Fennel, T. Shaaran, T. Zimmermann, A. Chacón, R. Guichard, A. Zaïr, J. W. G. Tisch, J. P. Marangos, T. Witting, A. Braun, S. A. Maier, L. Roso *et al.*, Attosecond physics at the nanoscale, *Rep. Prog. Phys.* **80**, 054401 (2017).
- [28] S. Y. Kruchinin, F. Krausz, and V. S. Yakovlev, Colloquium: Strong-field phenomena in periodic systems, *Rev. Mod. Phys.* **90**, 021002 (2018).
- [29] A. McPherson, G. Gibson, H. Jara, U. Johann, T. S. Luk, I. A. McIntyre, K. Boyer, and C. K. Rhodes, Studies of multiphoton production of vacuum-ultraviolet radiation in the rare gases, *J. Opt. Soc. Am. B* **4**, 595 (1987).
- [30] M. Ferray, A. L'Huillier, X. F. Li, L. A. Lompre, G. Mainfray, and C. Manus, Multiple-harmonic conversion of 1064 nm radiation in rare gases, *J. Phys. B* **21**, L31 (1988).
- [31] M. Lewenstein and A. L'Huillier, Principles of single atom physics: High-order harmonic generation, above-threshold ionization and non-sequential ionization, in *Strong Field Laser Physics*, Springer Series in Optical Sciences, edited by T. Brabec (Springer, New York, 2009), pp. 147–183.
- [32] J.-F. Hergott, M. Kovacev, H. Merdji, C. Hubert, Y. Mairesse, E. Jean, P. Breger, P. Agostini, B. Carré, and P. Salières,

- Extreme-ultraviolet high-order harmonic pulses in the micro-joule range, *Phys. Rev. A* **66**, 021801(R) (2002).
- [33] E. Constant, D. Garzella, P. Breger, E. Mével, C. Dorrer, C. Le Blanc, F. Salin, and P. Agostini, Optimizing High Harmonic Generation in Absorbing Gases: Model and Experiment, *Phys. Rev. Lett.* **82**, 1668 (1999).
- [34] C. M. Heyl, C. L. Arnold, A. Couairon, and A. L’Huillier, Introduction to macroscopic power scaling principles for high-order harmonic generation, *J. Phys. B* **50**, 013001 (2017).
- [35] S. M. Teichmann, F. Silva, S. L. Cousin, M. Hemmer, and J. Biegert, 0.5-keV soft x-ray attosecond continua, *Nat. Commun.* **7**, 11493 (2016).
- [36] D. Popmintchev, B. R. Galloway, M. C. Chen, F. Dollar, C. A. Mancuso, A. Hankla, L. Miaja-Avila, G. O’Neil, J. M. Shaw, G. Fan, S. Ališauskas, G. Andriukaitis, T. Balčiunas, O. D. Mücke, A. Pugzlys, A. Baltuška, H. C. Kapteyn, T. Popmintchev, and M. M. Murnane, Near- and Extended-Edge X-Ray-Absorption Fine-Structure Spectroscopy using Ultrafast Coherent High-Order Harmonic Supercontinua, *Phys. Rev. Lett.* **120**, 093002 (2018).
- [37] F. Krausz and M. Ivanov, Attosecond physics, *Rev. Mod. Phys.* **81**, 163 (2009).
- [38] Y. Kobayashi, T. Sekikawa, Y. Nabekawa, and S. Watanabe, 27-fs extreme ultraviolet pulse generation by high-order harmonics, *Opt. Lett.* **23**, 64 (1998).
- [39] K. Midorikawa, Y. Nabekawa, and A. Suda, XUV multiphoton processes with intense high-order harmonics, *Prog. Quantum Electron.* **32**, 43 (2008).
- [40] S. Chatziathanasiou, S. Kahaly, E. Skantzakis, G. Sansone, R. Lopez-Martens, S. Haessler, K. Varju, G. D. Tsakiris, D. Charalambidis, and P. Tzallas, Generation of attosecond light pulses from gas and solid state media, *Photonics* **4**, 26 (2017).
- [41] N. Tsatrafyllis, B. Bergues, H. Schröder, L. Veisz, E. Skantzakis, D. Gray, B. Bodi, S. Kuhn, G. D. Tsakiris, D. Charalambidis, and P. Tzallas, The ion microscope as a tool for quantitative measurements in the extreme ultraviolet, *Sci. Rep.* **6**, 21556 (2016).
- [42] B. Bergues, D. E. Rivas, M. Weidman, A. A. Muschet, W. Helml, A. Guggenmos, V. Pervak, U. Kleineberg, G. Marcus, R. Kienberger, D. Charalambidis, P. Tzallas, H. Schröder, F. Krausz, and L. Veisz, Tabletop nonlinear optics in the 100-eV spectral region, *Optica* **5**, 237 (2018).
- [43] A. Nayak, I. Orfanos, I. Makos, M. Dumergue, S. Kühn, E. Skantzakis, B. Bodi, K. Varju, C. Kalpouzos, H. I. B. Banks, A. Emmanouilidou, D. Charalambidis, and P. Tzallas, Multiple ionization of argon via multi-XUV-photon absorption induced by 20-GW high-order harmonic laser pulses, *Phys. Rev. A* **98**, 023426 (2018).
- [44] B. Senfftleben, M. Kretschmar, A. Hoffmann, M. Sauppe, J. Tümmler, I. Will, T. Nagy, M. J. J. Vrakking, D. Rupp, and B. Schütte, Highly non-linear ionization of atoms induced by intense high-harmonic pulses, *J. Phys.: Photon.* **2**, 034001 (2020).
- [45] I. Orfanos, I. Makos, I. Liontos, E. Skantzakis, B. Major, A. Nayak, M. Dumergue, S. Kühn, S. Kahaly, K. Varju, G. Sansone, B. Witzel, C. Kalpouzos, L. A. A. Nikolopoulos, P. Tzallas, and D. Charalambidis, Non-linear processes in the extreme ultraviolet, *J. Phys.: Photon.* **2**, 042003 (2020).
- [46] C. Gohle, T. Udem, M. Herrmann, J. Rauschenberger, R. Holzwarth, H. A. Schuessler, F. Krausz, and T. W. Hänsch, A frequency comb in the extreme ultraviolet, *Nature (London)* **436**, 234 (2005).
- [47] A. Cingöz, D. C. Yost, T. K. Allison, A. Ruehl, M. E. Fermann, I. Hartl, and J. Ye, Direct frequency comb spectroscopy in the extreme ultraviolet, *Nature (London)* **482**, 68 (2012).
- [48] L. Young, K. Ueda, M. Gühr, P. H. Bucksbaum, M. Simon, S. Mukamel, N. Rohringer, K. C. Prince, C. Masciovecchio, M. Meyer, A. Rudenko, D. Rolles, C. Bostedt, M. Fuchs, D. A. Reis, R. Santra, H. Kapteyn, M. Murnane, H. Ibrahim, F. Légaré *et al.*, Roadmap of ultrafast x-ray atomic and molecular physics, *J. Phys. B* **51**, 032003 (2018).
- [49] S. Fuchs, M. Wünsche, J. Nathanael, J. J. Abel, C. Rödel, J. Biedermann, J. Reinhard, U. Hübner, and G. G. Paulus, Optical coherence tomography with nanoscale axial resolution using a laser-driven high-harmonic source, *Optica* **4**, 903 (2017).
- [50] M. Lewenstein, M. F. Ciappina, E. Pisanty, J. Rivera-Dean, P. Stammer, T. Lamprou, and P. Tzallas, Generation of optical Schrödinger cat states in intense laser-matter interactions, *Nat. Phys.* **17**, 1104 (2021).
- [51] G. G. Paulus, W. Nicklich, H. Xu, P. Lambropoulos, and H. Walther, Plateau in Above Threshold Ionization Spectra, *Phys. Rev. Lett.* **72**, 2851 (1994).
- [52] A. Wünsche, Quantization of Gauss-Hermite and Gauss-Laguerre beams in free space, *J. Opt. B* **6**, S47 (2004).
- [53] T. Schultz and M. Vrakking, *Attosecond and XUV Physics: Ultrafast Dynamics and Spectroscopy* (Wiley, Weinheim, 2014).
- [54] D. Bauer and P. Koval, Qprop: A Schrödinger-solver for intense laser-atom interaction, *Comput. Phys. Commun.* **174**, 396 (2006).
- [55] G. Breitenbach, S. Schiller, and J. Mlynek, Measurement of the quantum states of squeezed light, *Nature (London)* **387**, 471 (1997).
- [56] A. I. Lvovsky and M. G. Raymer, Continuous-variable optical quantum-state tomography, *Rev. Mod. Phys.* **81**, 299 (2009).
- [57] N. Tsatrafyllis, I. K. Kominis, I. A. Gonoskov, and P. Tzallas, High-order harmonics measured by the photon statistics of the infrared driving-field exiting the atomic medium, *Nat. Commun.* **8**, 15170 (2017).
- [58] P. Stammer, J. Rivera-Dean, T. Lamprou, E. Pisanty, M. F. Ciappina, P. Tzallas, and M. Lewenstein, High Photon Number Entangled States and Coherent State Superposition from the Extreme-Ultraviolet to the Far Infrared, [arXiv:2107.12887](https://arxiv.org/abs/2107.12887) [Phys. Rev. Lett. (to be published)].
- [59] M. Brune, S. Haroche, J. M. Raimond, L. Davidovich, and N. Zagury, Manipulation of photons in a cavity by dispersive atom-field coupling: Quantum-nondemolition measurements and generation of “Schrödinger cat” states, *Phys. Rev. A* **45**, 5193 (1992).
- [60] S. Deléglise, I. Dotsenko, C. Sayrin, J. Bernu, M. Brune, J.-M. Raimond, and S. Haroche, Reconstruction of non-classical cavity field states with snapshots of their decoherence, *Nature (London)* **455**, 510 (2008).
- [61] J. Rivera-Dean, P. Stammer, E. Pisanty, T. Lamprou, P. Tzallas, M. Lewenstein, and M. F. Ciappina, New schemes for creating large optical Schrödinger cat states using strong laser fields, *J. Comput. Electron.* **20**, 2111 (2021).
- [62] M. Lewenstein, K. C. Kulander, K. J. Schafer, and P. H. Bucksbaum, Rings in above-threshold ionization: A quasiclassical analysis, *Phys. Rev. A* **51**, 1495 (1995).

- [63] N. Suárez, A. Chacón, M. F. Ciappina, J. Biegert, and M. Lewenstein, Above-threshold ionization and photoelectron spectra in atomic systems driven by strong laser fields, *Phys. Rev. A* **92**, 063421 (2015).
- [64] N. Suárez, A. Chacón, M. F. Ciappina, B. Wolter, J. Biegert, and M. Lewenstein, Above-threshold ionization and laser-induced electron diffraction in diatomic molecules, *Phys. Rev. A* **94**, 043423 (2016).
- [65] N. Suárez, A. Chacón, E. Pisanty, L. Ortmann, A. S. Landsman, A. Picón, J. Biegert, M. Lewenstein, and M. F. Ciappina, Above-threshold ionization in multicenter molecules: The role of the initial state, *Phys. Rev. A* **97**, 033415 (2018).
- [66] N. Tsatrafyllis, S. Kühn, M. Dumergue, P. Foldi, S. Kahaly, E. Cormier, I. Gonoskov, B. Kiss, K. Varju, S. Varro, and P. Tzallas, Quantum Optical Signatures in a Strong Laser Pulse After Interaction with Semiconductors, *Phys. Rev. Lett.* **122**, 193602 (2019).
- [67] U. Leonhardt, *Measuring the Quantum State of Light* (Cambridge University Press, Cambridge, 1997), Vol. 22.
- [68] U. Leonhardt, Quantum statistics of a lossless beam splitter: $Su(2)$ symmetry in phase space, *Phys. Rev. A* **48**, 3265 (1993).
- [69] J. Preskill, Quantum computing in the NISQ era and beyond, *Quantum* **2**, 79 (2018).
- [70] I. M. Georgescu, S. Ashhab, and F. Nori, Quantum simulation, *Rev. Mod. Phys.* **86**, 153 (2014).
- [71] E. Farhi, J. Goldstone, S. Gutmann, J. Lapan, A. Lundgren, and D. Preda, A quantum Adiabatic Evolution Algorithm Applied to Random Instances of an NP-Complete Problem, *Science* **292**, 472 (2001).
- [72] N. Gisin and R. Thew, Quantum communication, *Nat. Photon.* **1**, 165 (2007).
- [73] V. Giovannetti, S. Lloyd, and L. Maccone, Advances in quantum metrology, *Nat. Photon.* **5**, 222 (2011).
- [74] C. L. Degen, F. Reinhard, and P. Cappellaro, Quantum sensing, *Rev. Mod. Phys.* **89**, 035002 (2017).
- [75] T. Lamprou, R. Lopez-Martens, S. Haessler, I. Lontos, S. Kahaly, J. Rivera-Dean, P. Stammer, E. Pisanty, M. F. Ciappina, M. Lewenstein, and P. Tzallas, Quantum-optical spectrometry in relativistic laser-plasma interactions using the high-harmonic generation process: A proposal, *Photonics* **8**, 192 (2021).
- [76] J. Tannor, *Introduction to Quantum Mechanics: A Time-Dependent Perspective* (University Science Books, Sausalito, 2007).
- [77] A. Royer, Wigner function as the expectation value of a parity operator, *Phys. Rev. A* **15**, 449 (1977).
- [78] D. B. Milošević, G. G. Paulus, D. Bauer, and W. Becker, Above-threshold ionization by few-cycle pulses, *J. Phys. B* **39**, R203 (2006).
- [79] P. Stammer, J. Rivera-Dean, T. Lamprou, M. F. Ciappina, A. S. Maxwell, A. F. Ordóñez, E. Pisanty, P. Tzallas, and M. Lewenstein (unpublished).
- [80] G. van de Sand and J. M. Rost, Semiclassical description of multiphoton processes, *Phys. Rev. A* **62**, 053403 (2000).